國 立 交 通 大 學

電信工程學系

碩 士 論 文

適用於正交分頻多工行動系統之
都普勒偏移估測與干擾消除技術
Doppler Shift Estimation and Interference
Cancellation for Mobile OFDM Systems

研 究 生：李思漢   Student: Sih-Han Li

指導教授：李大嵩 博士   Advisor: Dr. Ta-Sung Lee

中 華 民 國 九 十 七 年 六 月

適用於正交分頻多工行動系統之都普勒偏移估測
與干擾消除技術

Doppler Shift Estimation and Interference Cancellation
for Mobile OFDM Systems

研 究 生：李思漢　　　　　　　Student: Sih-Han Li

指導教授：李大嵩 博士　　　　　Advisor: Dr. Ta-Sung Lee

國 立 交 通 大 學

電 信 工 程 學 系 碩 士 班

碩 士 論 文

A Thesis
Submitted to Department of Communication Engineering
College of Electrical Engineering and Computer Engineering
National Chiao Tung University
in Partial Fulfillment of the Requirements
for the Degree of
Master of Science
in
Communication Engineering
June 2008
Hsinchu, Taiwan, Republic of China

中 華 民 國 九 十 七 年 六 月

適用於正交分頻多工行動系統之都普勒偏移估測與干擾消除技術

研究生：李思漢　　　　　　　　　指導教授：李大嵩 博士

國立交通大學電信工程學系碩士班

摘要

　　近年來，正交分頻多工（Orthogonal Frequency Division Multiplexing, OFDM）系統在無線寬頻通訊之應用上日漸普及，許多系統與規格均採納此技術，例如數位電視、數位廣播、IEEE 802.11 a/g/n、IEEE 802.16 等。此外，移動傳輸將是未來無線通訊系統的趨勢之一，但正交分頻多工系統在移動的環境下將面臨都普勒偏移（Doppler Shift）的問題。都普勒偏移使得接收端的子載波間失去正交性，因而導致子載波間的相互干擾，並限制了系統的效能。為了解決此問題，在本篇論文中，吾人提出一個最大都普勒偏移的估測方法，此方法可良好地運作在低信噪比（Signal-to-Noise ratio, SNR）的環境下。且利用此估測出的都普勒資訊，吾人可使用一個適應性的干擾消除方法，選擇合適的等化器（Equalizer）來消去子載波的干擾，而不會浪費運算量。吾人也藉由電腦模擬來驗證所提方法可良好運作在正交分頻多工系統中。

Doppler Shift Estimation and Interference Cancellation for Mobile OFDM Systems

Student: Sih-Han Li   Advisor: Dr. Ta-Sung Lee

Department of Communication Engineering

National Chiao Tung University

Abstract

In recent years, orthogonal frequency division multiplexing (OFDM) becomes a popular technique in wireless broadband communications. There are many systems adopting OFDM techniques, such as digital video broadcasting (DVB), digital audio broadcasting (DAB), IEEE 802.11 a/g/n, IEEE 802.16, etc. On the other hand, mobile transmission is a trend in future wireless communications. However, in mobile OFDM systems, Doppler shift destroys the orthogonality between subcarriers, and this causes the intercarrier interference (ICI) and limits the performance of the receiver. To deal with this problem, we proposed a maximum Doppler shift estimation method for mobile OFDM systems, and the proposed method can work well at low SNR. Then, with the help of the Doppler information, an adaptive ICI cancellation scheme can be employed, which can choose an appropriate equalizer to cancel ICI without needing unnecessary computation. Finally, computer simulation results for mobile OFDM systems are included to confirm the proposed method.

Acknowledgement

I would like to express my deepest gratitude to my advisor, Dr. Ta-Sung Lee, for his enthusiastic guidance and great patience. I learn a lot from his positive attitude in many areas. Heartfelt thanks are also offered to all members in the Communication System Design and Signal Processing (CSDSP) Lab for their constant encouragement. Finally, I would like to show my sincere thanks to my parents for their invaluable love.

Contents

List of Figures

List of Tables

Acronyms Glossary

ACF	autocorrelation function
AWGN	additive white Gaussian noise
BER	bit-error-rate
CIR	channel impulse response
CP	cyclic prefix
CSI	channel state information
CTA	chirp transform algorithm
DFT	discrete Fourier transform
DAB	digital audio broadcasting
DVB-T	digital video broadcasting-terrestrial
FFT	fast Fourier transform
ICI	intercarrier interference
IDFT	inverse DFT
IFFT	inverse FFT
ISI	intersymbol interference
LS	least square
MCM	multi-carrier modulation
MMSE	minimum mean square error
MSE	mean square error
OFDM	orthogonal frequency division multiplexing
SNR	signal-to-noise ratio
WSSUS	wide sense stationary uncorrelated scattering

Notations

D	number of subcarrier of ICI mitigation
$\mathbf{F}$	DFT matrix
f_d	maximum Doppler shift
f_n	normalized maximum Doppler shift
$h_{n,l}$	time domain channel tap of l-th tap at time instance n
H_i	channel transfer function at the i-th subcarrier
$\mathbf{H}_{\mathrm{FD}}$	frequency domain channel matrix
$\mathbf{H}_{\mathrm{TD}}$	time domain channel matrix
I_i	ICI term at the i-th subcarrier
K	interval observation
L	length of channel
M	number of CTA output
ν	AWGN
N	number of subcarrier
N_{CP}	number of cyclic prefix
N_{P}	number of pilot tone
P_i	pilot tone at the i-th subcarrier
Q	accumulation size
τ	time delay
T_{s}	sampling period
T_{sym}	symbol duration
w	angel frequency
x	transmitted time domain signal
X	transmitted frequency domain signal
y	received signal before FFT

Y	received signal after FFT
$S\left(\cdot\right)$	Doppler power spectrum
$\phi_{hh}\left(\cdot\right)$	autocorrelation of consecutive CIRs
$J_0\left(\cdot\right)$	zeroth order Bessel function of the first kind
$\left(\cdot\right)^*$	complex conjugate
$\left(\cdot\right)^H$	complex conjugate transpose
$\left(\cdot\right)^{-1}$	inverse
$\arg\left(\cdot\right)$	argument
$\max\left(\cdot\right)$	maximum
$\mathrm{DFT}\left\{\cdot\right\}$	DFT
$E\left\{\cdot\right\}$	expectation
$\mathrm{FT}\left\{\cdot\right\}$	Fourier transform
$\mathrm{FFT}\left\{\cdot\right\}$	FFT
$\mathrm{IDFT}\left\{\cdot\right\}$	IDFT
$\mathrm{IFFT}\left\{\cdot\right\}$	IFFT

Chapter 1

Introduction

Orthogonal frequency division multiplexing (OFDM) is a popular technique in modern wireless broadband communication systems. Nowadays, OFDM is utilized in many standards. In wired transmission systems, OFDM is adopted in asymmetric digital subscriber loop (ADSL) and very high bit-rate digital subscriber loop (VDSL). In wireless transmission systems, OFDM is utilized in digital audio broadcasting-terrestrial (DVB-T) [1], [2], [3], digital audio broadcasting-handheld (DVB-H) [4], digital audio broadcasting (DAB), IEEE 802.11 a/g/n, and IEEE 802.16, etc. In OFDM systems, the available bandwidth is divided into several orthogonal subcarriers for transmission. Then, a cyclic prefix (CP) is inserted before each transmitted OFDM symbol. If the length of CP is equal to or longer than the delay spread of the channel, the intersymbol interference (ISI) can be eliminated. Moreover, subcarriers in OFDM systems are orthogonal to each other over time-invariant channels, thus the conventional OFDM systems could only utilize a simple one-tap equalizer to recover the transmitted symbol on each subcarrier [5].

In wireless environments, because of the user's movement, the channel is time variant. The user's mobility introduces a Doppler shift, which destroyed the orthogonality between subcarriers and degraded the bit-error-rate (BER) performance. In time varying channels, the conventional one-tap equalizer in OFDM systems is

insufficient. Therefore, in order to improve the BER performance, the ICI cancellation technique plays a very important role in mobile OFDM systems. To mitigate ICI in an efficient manner, it is necessary to know the value of the maximum Doppler shift. With the help of the Doppler information, an appropriate equalizer can be chosen to cancel ICI without needing unnecessary computation.

Many methods have been proposed to estimate the maximum Doppler shift. The autocorrelation function (ACF) based Doppler shift estimation method has been proposed in [6]. A maximum-likelihood (ML) approach based estimation is exploited in [7], [8]. However, these methods are sensitive to signal-to-noise ratio (SNR). In OFDM systems, the autocorrelation between the repeated parts of the symbol due to CP has been exploited in [9] to estimate the maximum Doppler shift. When the environment causes long delay spread, the estimation will degrade greatly. Moreover, this method is also sensitive to SNR. To deal with the noise problem, a method, which uses the channel power spectrum, is described in [10].

The main topic of this thesis is about the maximum Doppler shift estimation method for OFDM systems. Since the Doppler power spectrum is related to the maximum Doppler shift, a maximum Doppler shift estimation method which utilizes the Doppler power spectrum is proposed in this thesis. By exploiting the characteristics of the Doppler power spectrum, the ACF of the estimated channel impulse response (CIR) at the receiver is translated onto the frequency domain by Fourier transform. Two kinds of Fourier transform schemes will be introduced; one is fast Fourier transform (FFT) scheme, and the other is chirp transform algorithm (CTA) scheme. These schemes provide a tradeoff between computational complexity and memory size. Furthermore, because of using the autocorrelation of the channel impulse responses, the proposed method is robust to SNR variation. Next, by using the estimated maximum

Doppler shift, an adaptive ICI cancellation scheme is proposed. The estimated maximum Doppler shift is utilized as a parameter of the adaptive ICI cancellation scheme, and the parameter can help in selecting the appropriate equalizer technique. In order to mitigate the ICI effectively, a conventional linear minimum mean square error (MMSE) equalizer [11], [12] can be employed. The complexity of the conventional MMSE equalizer requires $O\left(N^3\right)$ operations, resulting in impractical implementation for large N. Therefore, a low-complexity MMSE equalizer [5] is utilized in this thesis to reduce the computational complexity. DVB-T is selected as the system platform for computer simulations.

The remainder of this thesis is organized as follows. Chapter 2 provides the overview of OFDM systems and DVB-T systems. In Chapter 3, the proposed maximum Doppler shift estimation method is presented and analyzed. In Chapter 4, ICI analysis is introduced and an adaptive ICI cancellation scheme is discussed. In Chapter 5, we conclude this thesis and propose some potential future works.
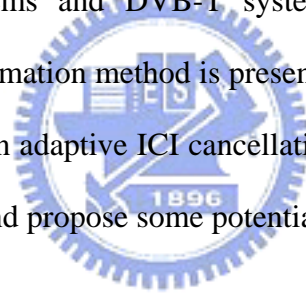
Chapter 2

Fundamentals of OFDM and DVB-T Systems

In this chapter, we discuss the technique of orthogonal frequency division multiplexing (OFDM) and a digital video broadcasting system based on OFDM technique. First, we state the principle of OFDM transmission and its block diagram. Then, we will make a description of digital video broadcasting-terrestrial (DVB-T) standard including the system block diagram, frame structure, and reference signal.
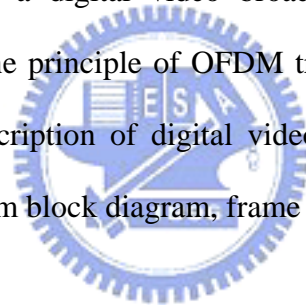
2.1 Overview of OFDM Systems

OFDM derived from multi-carrier modulation (MCM) [13] which is a technique of transmitting high-speed data by dividing the stream into several parallel low-rate streams and modulating each of these data streams onto individual subcarriers, as shown in Figure 2.1. Therefore, by making all subcarriers of MCM narrowband, each subcarrier experiences almost flat fading, which makes equalization very simple.
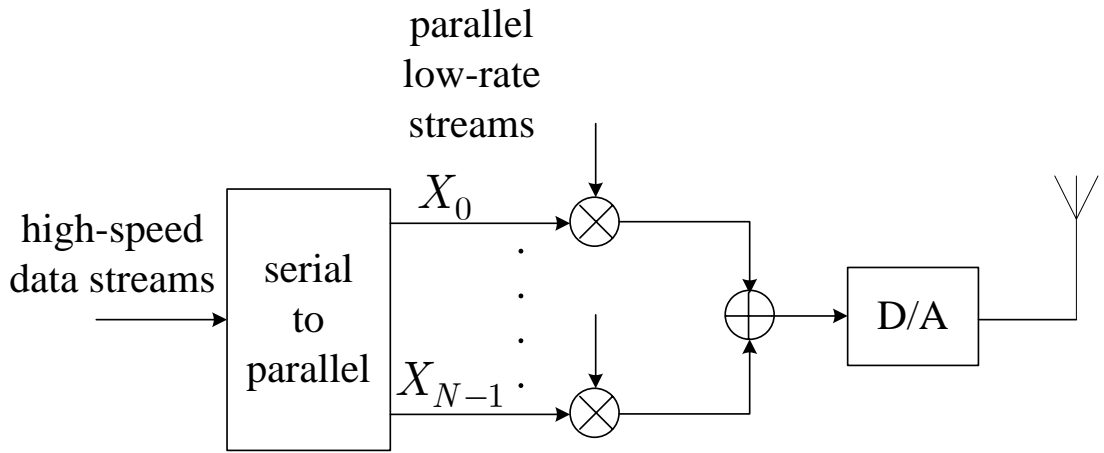
Figure 2.1: MCM scheme for high-speed transmission

Compared with MCM systems, the subcarriers of OFDM systems are overlapping and orthogonal to each other. For two subcarriers to be orthogonal within $[0, T]$, they must be satisfy the orthogonality constraint:

$$\int_0^T w_n\,(t) \cdot w_k^*\,(t)\,dt = \begin{cases} 1, & n = k \\ 0, & n \neq k \end{cases}.$$ (2.1)

With the property of orthogonality, Figure 2.2 shows OFDM systems have better bandwidth efficiency than traditional MCM systems. The spectra of OFDM signals are depicted in Figure 2.3. The overlapping *sinc* shaped spectra have zero inter-subcarrier interference at the right frequency sampling points.
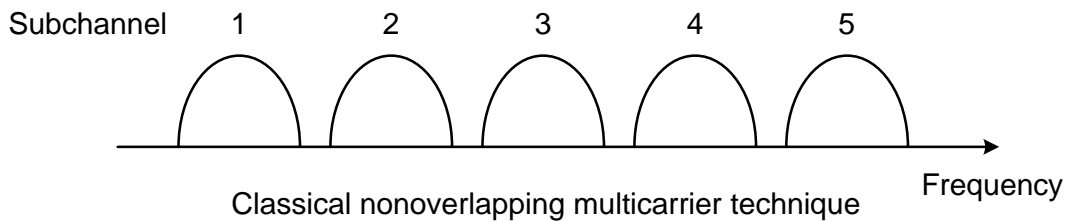
Figure 2.2 (a): Illustration of OFDM bandwidth efficiency: traditional MCM technique
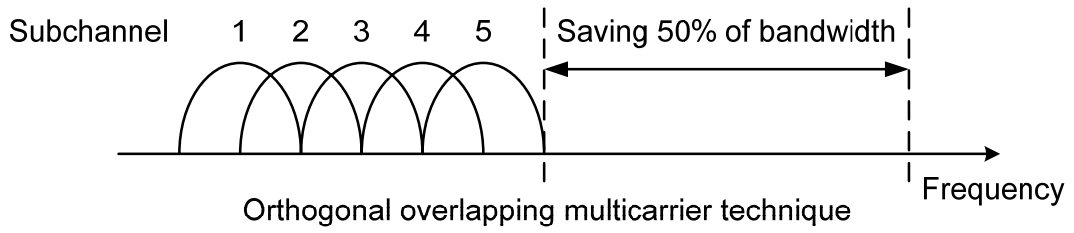
Figure 2.2 (b): Illustration of OFDM bandwidth efficiency: OFDM technique
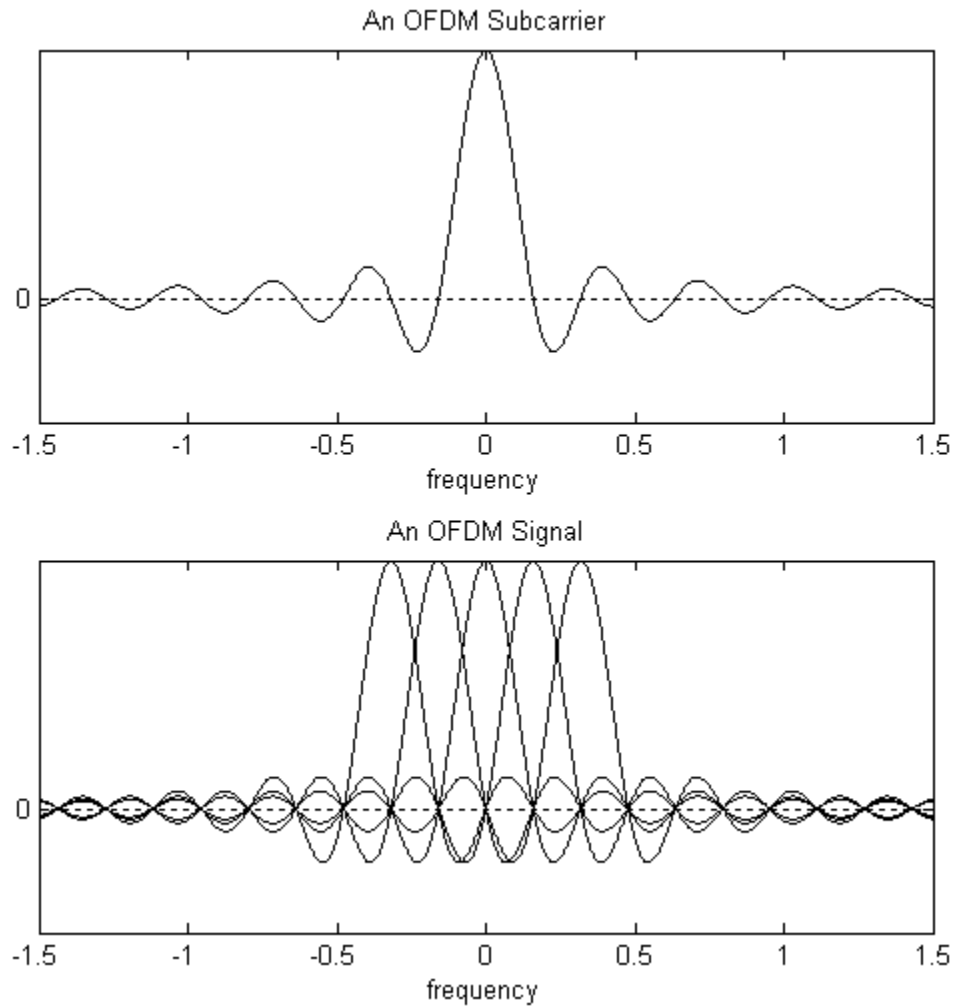
Figure 2.3: OFDM signal spectra

2.1.1 Guard Interval and Cyclic Prefix (CP)

Although the problem of multipath fading may be dealt with efficiently in OFDM systems, however, as in single carrier systems, intersymbol interference (ISI) is still a major concern for OFDM systems, as shown in Figure 2.4(a). In order to combat ISI, Figure 2.4(b) shows a zero-padded guard interval is introduced for each OFDM symbol. The guard interval is set larger than the multipath delay spread, such that the pervious symbol cannot interfere with the current symbol. However, intercarrier interference (ICI) arises because of the zero-padded guard interval.
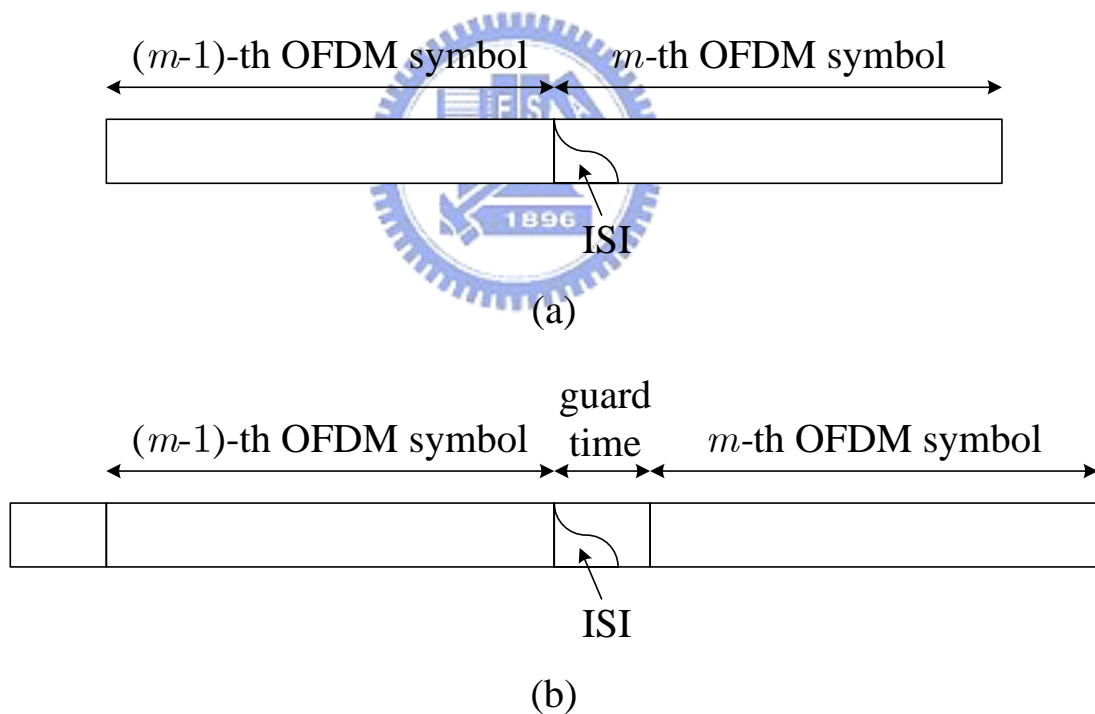
Figure 2.4: ISI phenomenon of OFDM systems: (a) without guard interval, (b) zero-padded guard interval

ICI is crosstalk between different subcarriers, which means that the orthogonality between subcarriers disappeared. To eliminate this obstacle, a cyclic prefix (CP) is introduced in the guard interval. Figure 2.5 illustrates this technique. CP ensures that there are always an integer number of cycles within a FFT interval, therefore the orthogonality between subcarriers can be held.
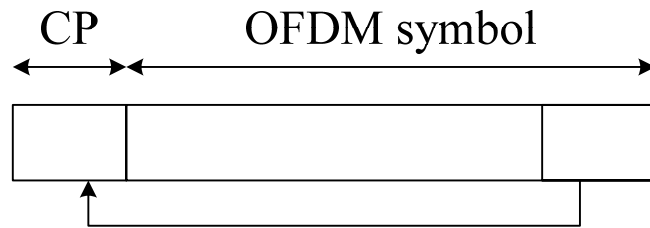
Figure 2.5: Guard interval with cyclic prefix

2.1.2 Continuous Time Model of OFDM

The general form of continuous time model of an OFDM signal can be written as a set of modulated carriers transmitted in parallel as follows

$$x_m(t) = \sum_{k=0}^{N-1} X_{k,m} \cdot w_k\left(t - mT_{\text{sym}}\right), \tag{2.2}$$

where

$$w_k(t) = \begin{cases} e^{j2\pi f_k t} & \text{for } t \in \left[0,\ T_{\text{sym}}\right) \\ 0 & \text{otherwise} \end{cases} \tag{2.3}$$

is the waveforms of the k-th subcarrier, and $f_k = f_0 + k/T_{\text{sym}}$, $k = 0, 1, 2, \cdots, N-1$. In this model, N is the number of subcarriers, $X_{k,m}$ is the transmitted data on the k-th subcarriers in the m-th OFDM symbol, T_{sym} is symbol period, and f_k is the carrier frequency of the k-th subcarrier. Consequently, a transmitted stream of OFDM symbols can be generally expressed as

$$x(t) = \sum_{m=-\infty}^{+\infty} x_m(t) = \sum_{m=-\infty}^{+\infty} \sum_{k=0}^{N-1} X_{k,m} \cdot w_k(t - mT_s). \tag{2.4}$$

For simplicity, assuming the channel is ideal, and the demodulation of OFDM is based on the orthogonality constraint in Equation (2.1), and therefore the demodulator may derive

$$\widehat{X}_{k,m} = \frac{1}{T} \int_{mT_s}^{(m+1)T_s} x(t) \cdot w_k^*(t) \, dt, \tag{2.5}$$

where $\widehat{X}_{k,m}$ is the received data on the subcarrier k-th in the m-th symbol. Figure 2.6 shows a simple transmission and reception processes of continuous time OFDM system model.
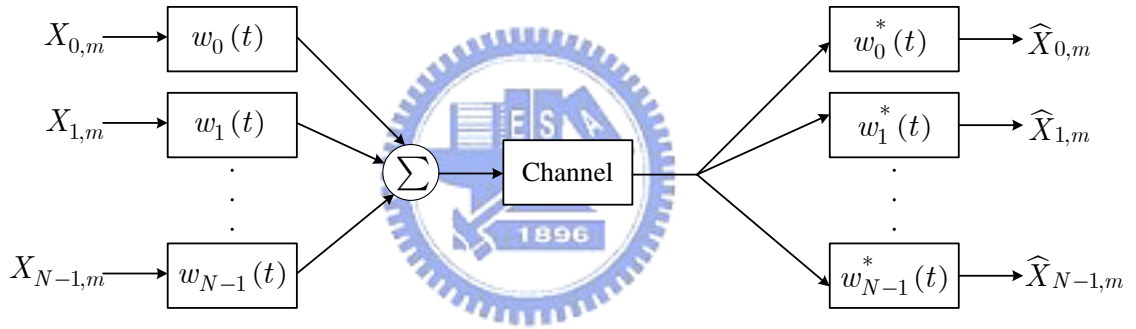
Figure 2.6: Continuous time OFDM system model

2.1.3 Discrete-Time Model of OFDM

Compare to the continuous time model, the modulator and demodulator of the discrete-time OFDM system are replaced by an inverse discrete Fourier transform (IDFT) and a discrete Fourier transform (DFT), respectively. In real implementation of an OFDM system, DFT is replaced by an appropriately sized fast Fourier transform (FFT) to reduce calculating complexity. The discrete-time OFDM system model can be written as

$$\widehat{\mathbf{X}}_m = \mathrm{DFT}\big(\mathrm{IDFT}(\mathbf{X}_m)\big), \tag{2.6}$$

where $\widehat{\mathbf{X}}_m = \begin{bmatrix} X_{0,m} & X_{1,m} & \cdots & X_{N-1,m} \end{bmatrix}$, and $\mathbf{X}_m$ contains N transmitted data in the m-th symbol. Figure 2.7 shows a simple transmission and reception processes of discrete-time OFDM system model.
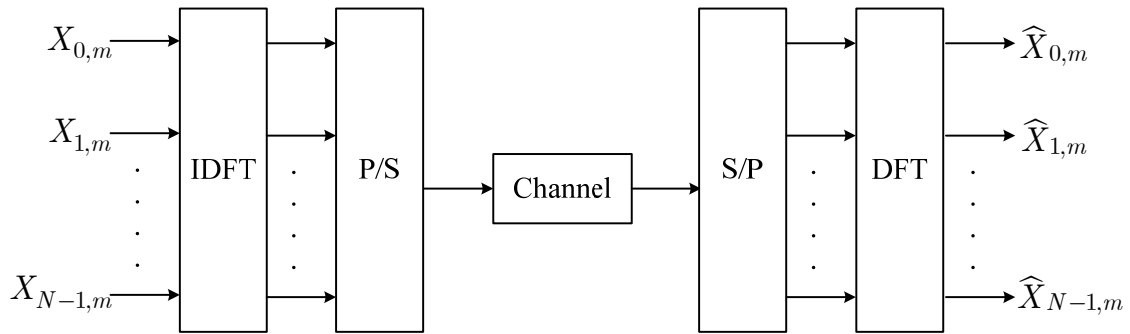
Figure 2.7: Discrete-time OFDM system model

2.2 Overview of DVB-T Systems

Digital video broadcasting–terrestrial (DVB-T) standard [1] based on coded OFDM (COFDM) and it was established by European Telecommunication Standard Institute (ETSI) in 1997. Furthermore, DVB-T is adopted by most countries around the world including Taiwan.

2.2.1 System Overview

Figure 2.8 depicts the functional block diagram of DVB-T system [14], [15]. The source coding of audio and video signals is based on ISO MPEG-2 standard. After the MPEG-2 transport multiplexer, the video, audio and data stream are translated to packets. The packet length is 188 bytes and it includes one synchronization word (sync-word, or $SYNC$) bytes and 187 data bytes. When the transmitting packet has priority, hierarchical transmission would be used. The splitter is used to split the packet

into high priority and low priority parts. These two parts of data could have individual channel coding and mapping mode. Every eight packet are multiplied by a pseudo random binary sequence (PRBS) which derived by the polynomial $X^{15} + X^{14} + 1$. To provide an initialization signal, the sync-word of the first packet in a group of eight packets is translated form 47_{HEX} (SYNC) to $B8_{HEX}$ ($\overline{SYNC}$). This operation is called multiplex adaptation and randomization for energy dispersal.
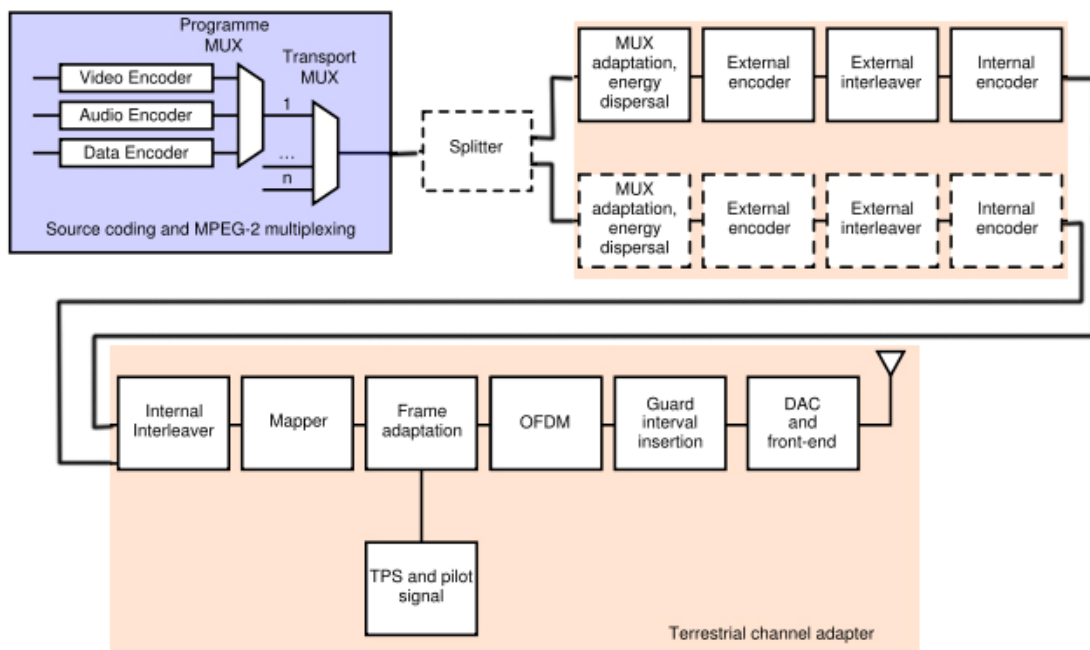
Figure 2.8: Functional block diagram of DVB-T

After multiplex adaptation, a Reed-Solomon (RS) shortened code (204, 188, t = 8) and a convolutional byte-wise interleaving with depth I = 12 shall be applied to generate error protected packets. The inner coder is designed for a range of punctured convolutional codes, which allows code rate of 1/2, 2/3, 3/4, 5/6, and 7/8. If hierarchical transmission is used, each of two parallel inner codes has its own code rate. Then, the inner interleaver is block based bit-wise interleaving. After channel coding and interleaving, the mapping modes are QPSK, 16-QAM, 64-QAM, non-uniform

16-QAM, and non-uniform 64-QAM where the "non-uniform" constellation level is used by hierarchical transmission. Moreover, the transmission channel bandwidth is 6 MHz, 7 MHz, and 8 MHz, respectively.

The DVB-T system based on OFDM technique with various transmission parameters. Two transmission modes are defined: a 2k mode and an 8k mode. The 2k mode is suitable for short distance and high mobility transmission because of its short symbol duration and wide sucarrier spacing. On the other hand, the 8k mode is suitable for long distance transmission and deep multipath delay spread. Other parameters such as code rate of inner coder, mapping mode, and length of guard interval would be determined properly according to the channel condition. The Table 2.1 lists the parameters in the 2k and 8k modes for 6 MHz channel bandwidth in DVB-T standard.

Table 2.1: Parameters for 6 MHz channel in DVB-T
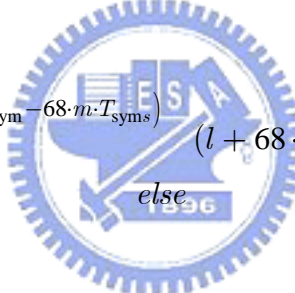
	8k mode	2k mode
Number of subcarriers	6817	1705
Value of carrier number $K_{\min}$	0	0
Value of carrier number $K_{\max}$	6816	1704
Carrier spacing $1/T_u$	837.054 Hz	3,348.214 Hz
Duration $T_u = Ts - T_{CP}$	1194.667 μs	298.6667 μs
Spacing between carriers $K_{\min}$ and $K_{\max}$	5.71 MHz	5.71 MHz
T_{CP}/T_u	$\frac{1}{4},\frac{1}{8},\frac{1}{16},\frac{1}{32}$	$\frac{1}{4},\frac{1}{8},\frac{1}{16},\frac{1}{32}$

2.2.2 Frame Structure and Transmission Band

The transmitted data is organized in frames. Each frame consists of 68 OFDM symbols and duration of a symbol is T_{sym}. Each symbol is constituted by a set of 6817 and 1705 carriers in the 8k and 2k mode, respectively. Therefore, the carrier are indexed by $k \in [K_{\min}; K_{\max}]$ and determined by $K_{\min} = 0$ and $K_{\max} = 6816$ in 8k mode and $K_{\max} = 1705$ in 2k mode. The emitted signal at time t is described by the following expression:

$$s(t) = \text{Re} \left\{ e^{j2\pi f_c t} \sum_{m=0}^{\infty} \sum_{l=0}^{67} \sum_{K_{\min}}^{K_{\max}} c_{m,l,k} \cdot w_{m,l,k}(t) \right\}, \tag{2.7}$$

where

$$w_{m,l,k}(t) = \begin{cases} e^{j2\pi \frac{k'}{T_U}(t - \Delta - l \cdot T_{\text{sym}} - 68 \cdot m \cdot T_{\text{syms}})} & (l + 68 \cdot m) \cdot T_{\text{sym}} \leq t \leq (l + 68 \cdot m + 1) \cdot T_{\text{sym}} \\ 0 & else \end{cases}$$

and $k' = k - (K_{\max} + K_{\min})/2$. In Equation (2.7), f_c denotes the central frequency of RF signal, m is the transmission frame number, l is the OFDM symbol number, k is the carrier number, $c_{m,l,k}$ the complex symbol for carrier k of the l-th data symbol in frame m, T_U is the inverse of the carrier spacing, and Δ is the duration of the guard interval.

The system is supposed to use the conventional analog broadcasting ultra high frequency (UHF) band with 8 MHz bandwidth. The central frequency f_c of RF signal is

$$f_c = 470 \text{ MHz} + 4 \text{ MHz} + i \cdot 8 \text{ MHz}, \quad i = 0, 1, 2, \cdots. \tag{2.8}$$

However, some countries define the transmission bandwidth as 6 MHz or 7 MHz. we could only change the sampling period to satisfy the regulated bandwidth. The sampling period T_s is $7/64\,\mu s$ for 8 MHz channels, $1/8\,\mu s$ for 7 MHz channels, and $7/48\,\mu s$ for 6 MHz channels.

2.2.3 Reference Signals

The main functions of reference signals are synchronization, channel estimation, and signaling. DVB-T has three kinds of reference signal: continual pilot, scattered pilot, and transmission reference signaling (TPS). The continual and scattered pilots are derived from a PRBS $W_k = X^{11} + X^2 + 1$.

- *Continual Pilot*

There are 177 continual pilots in the 8k mode and 45 continual pilots in the 2k mode. The continual pilots are placed into fixed subcarrier in every OFDM symbol as shown in Figure 2.9. The value of continual pilots on subcarrier k is given by

$$\mathrm{Re}\left\{c_{m,l,k}\right\} = 4/3 \times 2\left(1/2 - W_k\right), \tag{2.9}$$

and

$$\mathrm{Im}\left\{c_{m,l,k}\right\} = 0. \tag{2.10}$$

Where m is the transmission frame number, l is the OFDM symbol number, and k is the carrier number. The continual pilots are always transmitted at the boosted power level so that for these

$$E\left\{c \times c^*\right\} = 16/9, \tag{2.11}$$

where $(\cdot)^*$ denotes the complex conjugate.
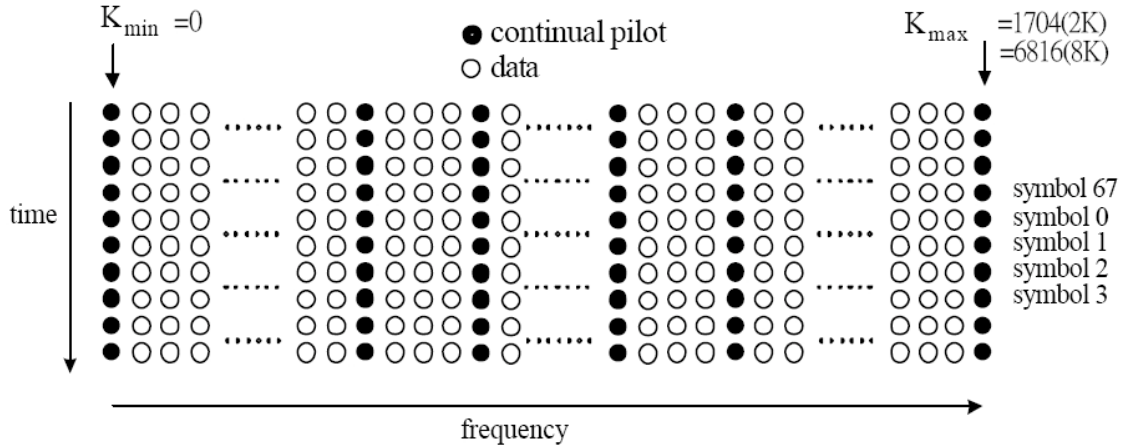
Figure 2.9: Continual pilot of DVB-T

● *Scattered Pilot*

Unlike the continual pilots, the scattered pilots are located at different subcarrier indices in every symbol. For the l-th OFDM symbol, the positions of the scattered pilots are

$$\left\{ k_p = K_{\min} + 3 \times (1 \mod 4) + 12i \mid i \text{ integer}, i \geq 0, k_p \in \left[K_{\min}; K_{\max} \right] \right\}. (2.12)$$

The values of scattered pilots with subcarrier k_p are produced in the same way with continual pilots in Equation (2.9) and Equation (2.10). Figure 2.10 shows the location of scattered pilots. There is a repetition for the location of scattered pilots every four OFDM symbols, so the scattered pilots have a period $P_t = 4$ in time domain. In frequency domain, the location of scattered pilots repeats every twelve subcarriers so that the period is $P_f = 12$.
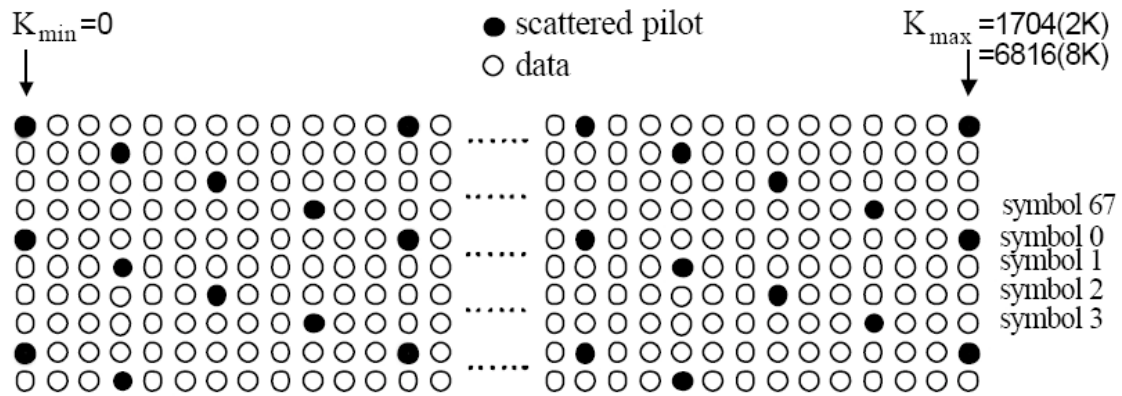
Figure 2.10: Scattered pilot of DVB-T

● *Transmission Parameter Signaling (TPS)*

The TPS carriers are used for the purpose of signaling parameters related to the transmission scheme, coding and modulation. There are 68 TPS carriers and 17 TPS carriers for 8k and 2k mode, respectively. Every TPS carrier in the same symbol informs the same differentially encoded information bit. The TPS carriers convey information on the following:

1) mapping mode;

2) hierarchy information;

3) length of guard interval;

4) inner code rates;

5) transmission mode;

6) frame number in a super-frame;

7) cell identification.

Chapter 3

Proposed Maximum Doppler Shift Estimation Method

In this chapter, a Doppler shift estimation method in digital mobile communication systems is described. The proposed method uses the Fourier transform of the autocorrelation function (ACF) of the channel impulse response (CIR), which is related with the maximum Doppler shift. By utilizing the characteristic of the Doppler power spectrum, the ACF of the CIR is translated into the frequency domain. Thus, we will introduce two schemes of Fourier transform, which are fast Fourier transform (FFT) and chirp transform algorithm (CTA). Moreover, we also analyze the complexity of these two schemes, which provide a tradeoff between computational complexity and memory size. Compared with the autocorrelation based Doppler shift estimation method [6], the proposed method which works in frequency domain is more robust to noisy environment. Therefore, the proposed method can work well at low signal-to-noise ratio (SNR).

Section 3.1 presents the OFDM system model and the channel model. In Section 3.2, the proposed maximum Doppler shift estimation method is described. The complexity analyses of FFT and CTA are provided in Section 3.3. Finally, the computer simulations and the summary are shown in Section 3.4 and Section 3.5, respectively.

3.1 System and Channel Models

Consider the OFDM system model, which is illustrated in Figure 3.1. A set of N-coded frequency domain symbols $\{X_k\}$ is collected to form an OFDM symbol $\mathbf{X} = \begin{bmatrix} X_0, & X_1, & \cdots, & X_{N-1} \end{bmatrix}^T$. And then, the OFDM symbol is converted into time domain samples $\{x_n\}$ according the N-point IFFT operation

$$x_n = \text{IFFT}\{\mathbf{X}\} \tag{3.1}$$

$$= \frac{1}{\sqrt{N}} \sum_{k=0}^{N-1} X_k e^{j2\pi nk/N}, \quad -N_{\text{CP}} \leq n \leq N-1 \tag{3.2}$$

where N_{CP} denotes the length of cyclic prefix (CP).
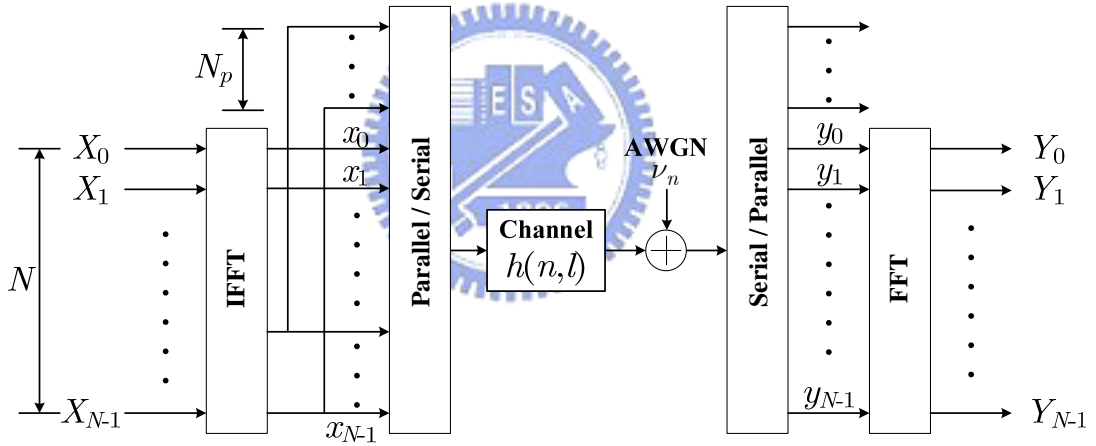
Figure 3.1: OFDM system model

The multipath channel is assumed to be time-variant, and the normalized length of the channel, L, is equal to or less than N_{CP}. Consequently, during an OFDM symbol period, the discrete-time channel impulse response is given by [16]

$$h(n,l) = \sum_{l=0}^{L-1} h_{n,l} \cdot \delta(n - \tau_l) \tag{3.3}$$

where $h_{n,l}$ is the channel response of the l-th tap at time instance n, and τ_l is delay spread of l-th tap. In this thesis, channel model is the typical wide sense stationary

uncorrelated scattering (WSSUS) model [17], [18], which will be described in detail later in Section 3.1.1. After transmitting through the channel, the received samples are collected during an OFDM symbol interval:

$$y_n = h(n,l) * x_n + \nu_n \tag{3.4}$$

$$= \sum_{l=0}^{L-1} h_{n,l} \cdot x_{n-l} + \nu_n, \ 0 \leq n \leq N-1 \tag{3.5}$$

where $*$ denotes convolution, and ν_n are samples of additive white Gaussian noise (AWGN) with variance $\sigma_{\nu_n}^2$. Perfect timing synchronization is assumed in this thesis. Due to the presence of the guard interval, the received signal is not corrupted by ISI in the range $0 \leq n \leq N-1$. Therefore, Equation (3.5) can be rewrite as

$$y_n = \sum_{l=0}^{L-1} h_{n,l} \cdot \left(\frac{1}{\sqrt{N}} \sum_{k=0}^{N-1} X_k e^{j2\pi(n-l)k/N} \right) + \nu_n$$

$$= \frac{1}{\sqrt{N}} \sum_{k=0}^{N-1} X_k e^{j2\pi nk/N} \sum_{l=0}^{L-1} h_{n,l} e^{j2\pi lk/N} + \nu_n, \ 0 \leq n \leq N-1. \tag{3.6}$$

By defining $H_k(n) = \sum_{l=0}^{L-1} h_{n,l} e^{j2\pi lk/N}$, which is Fourier transform of the CIR at time n. Then, Equation (3.6) can be expressed as

$$y_n = \frac{1}{\sqrt{N}} \sum_{k=0}^{N-1} H_k(n) \cdot X_k e^{j2\pi nk/N} + \nu_n, \ 0 \leq n \leq N-1. \tag{3.7}$$

Comparing Equation (3.7) with the transmitted signal X_k, we can find that the time-varying multipath channel introduces a time-varying complex multiplier, $H_k[n]$, at each subcarrier. Thus, after removing the ISI corrupted guard interval, the k-th subcarrier output from the FFT can be written as

$$Y_k = \frac{1}{\sqrt{N}} \sum_{n=0}^{N-1} y_n e^{-j2\pi nk/N} \tag{3.8}$$

$$= H_k X_k + I_k + V_k, \ 0 \leq k \leq N-1, \tag{3.9}$$

where

$$H_k = \frac{1}{N} \cdot \sum_{n=0}^{N-1} H_k(n), \tag{3.10}$$

$$I_k = \frac{1}{N} \cdot \sum_{\substack{m=0 \\ m \neq k}}^{N-1} X_m \sum_{n=0}^{N-1} H_m(n) e^{j2\pi n(m-k)/N}, \tag{3.11}$$

and

$$V_k = \frac{1}{\sqrt{N}} \cdot \sum_{n=0}^{N-1} \nu_n e^{j2\pi nk/N}. \tag{3.12}$$

In Equation (3.9), H_k is the channel transfer function at the k-th subcarrier, I_k is the ICI term, and V_k represents the AWGN.

3.1.1 Channel Model

The well-known WSSUS model [17], [18] is assumed in this thesis. Under this assumption, the ACF of the channel impulse response for l-th tap is given by [19]

$$\phi_{hh}(\tau) \equiv E\left\{ h_{n,l} \cdot h^*_{(n+\tau),l} \right\} = J_0\left(2\pi f_{d,l}\tau\right) \tag{3.13}$$

where $J_0(\cdot)$ is the zeroth order Bessel function of the first kind, and $f_{d,l}$ is the maximum Doppler shift. Figure 3.2 shows the theoretical value of the autocorrelation function ϕ_{hh} versus time delay. From this figure, we can know that maximum Doppler shift $f_{d,l}$ multiplied by time delay τ is constant. Thus, $f_{d,l}$ and τ have a reciprocal relationship. Moreover, the maximum Doppler shift $f_{d,l}$ is determined by the mobile velocity and the wavelength of carrier wave. Table 3.1 lists the maximum Doppler shift with different velocity for DVB-T systems.
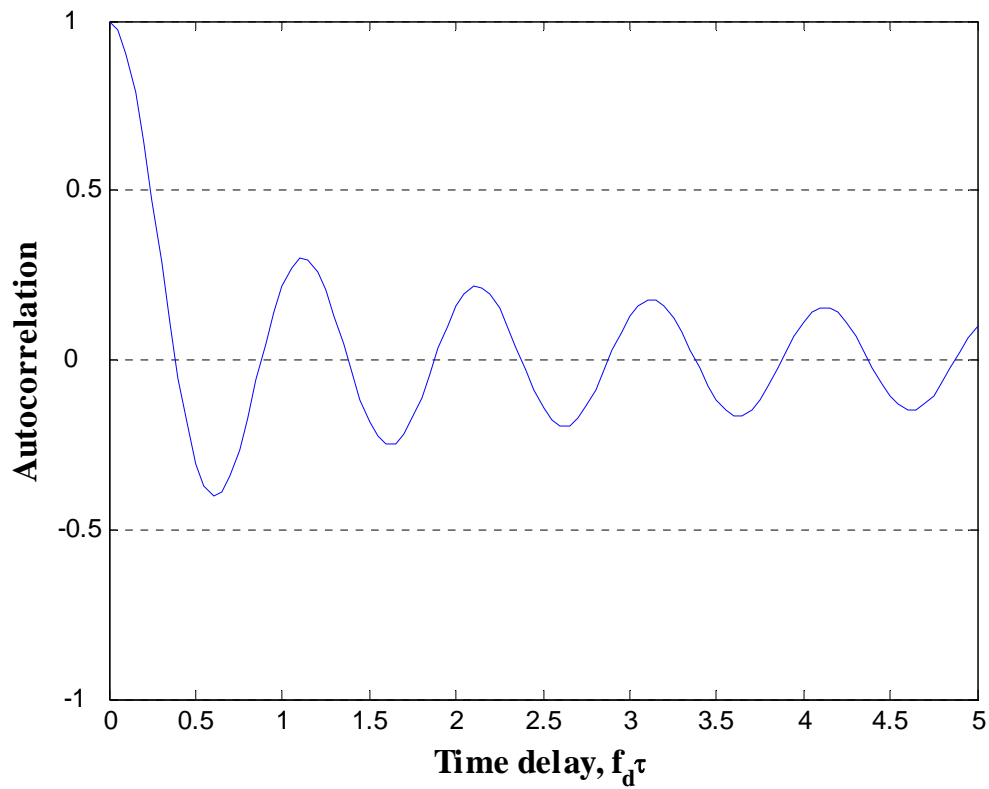
Figure 3.2: Autocorrelation function of the channel impulse response

Table 3.1: Maximum Doppler shift with different velocity for DVB-T systems

Carrier frequency: 584 MHz ~ 710 MHz	
Velocity	Maximum Doppler shift
50 km/hr	27.04 Hz ~ 32.87 Hz
100 km/hr	54.07 Hz ~ 65.74 Hz
150 km/hr	81.11 Hz ~ 98.61 Hz
200 km/hr	108.15 Hz ~ 131.48 Hz
300 km/hr	162.22 Hz ~ 197.22 Hz
400 km/hr	216.30 Hz ~ 262.96 Hz

The Fourier transform of Equation (3.13) denotes the Doppler power spectrum. In the case of Rayleigh fading, the Doppler power spectrum can be expressed as [17], [20]

$$S(f) = \text{FT}\left\{\phi_{hh}(\tau)\right\} = \begin{cases} \dfrac{1}{\pi f_{d,l} \cdot \sqrt{1 - \left(\dfrac{f}{f_{d,l}}\right)^2}}, & |f| \leq f_{d,l}, \\ 0, & |f| > f_{d,l}. \end{cases} \tag{3.14}$$

where T_s is the sampling time. Figure 3.3 depicts the Doppler power spectrum $S(f)$. Moreover, in this figure we can find that the position of peak corresponds to the maximum Doppler shift. Therefore, we can use this characteristic to estimate maximum Doppler shift.
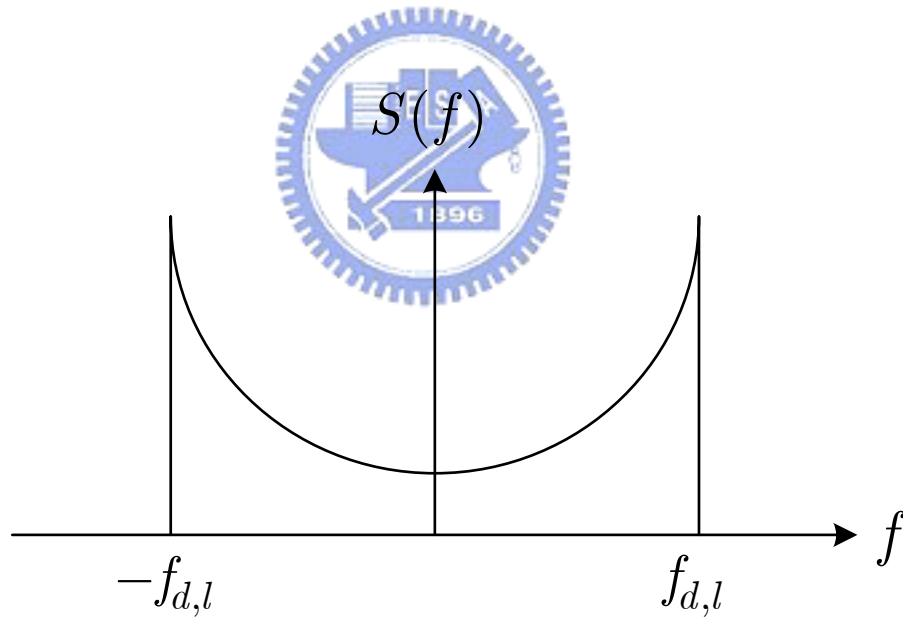
Figure 3.3: Illustration of Doppler power spectrum

3.2 Proposed Doppler Shift Estimation Method Using Doppler Power Spectrum

In this section, the procedure of proposed maximum Doppler shift estimation method is introduced. First, we use pilot tones to estimate the CIR. After an observation interval with K OFDM symbols, the consecutive estimated CIRs are used to compute the ACF. And then, we translate the ACF into the frequency domain. Therefore, the Doppler power spectrum of estimated CIRs is obtained. In order to improve the estimated accuracy of the maximum Doppler shift estimation, we could average some Doppler power spectrum estimated results. Then, using the estimated Doppler power spectrum finds the maximum Doppler shift. Figure 3.4 shows a block diagram of proposed maximum Doppler shift estimation method.
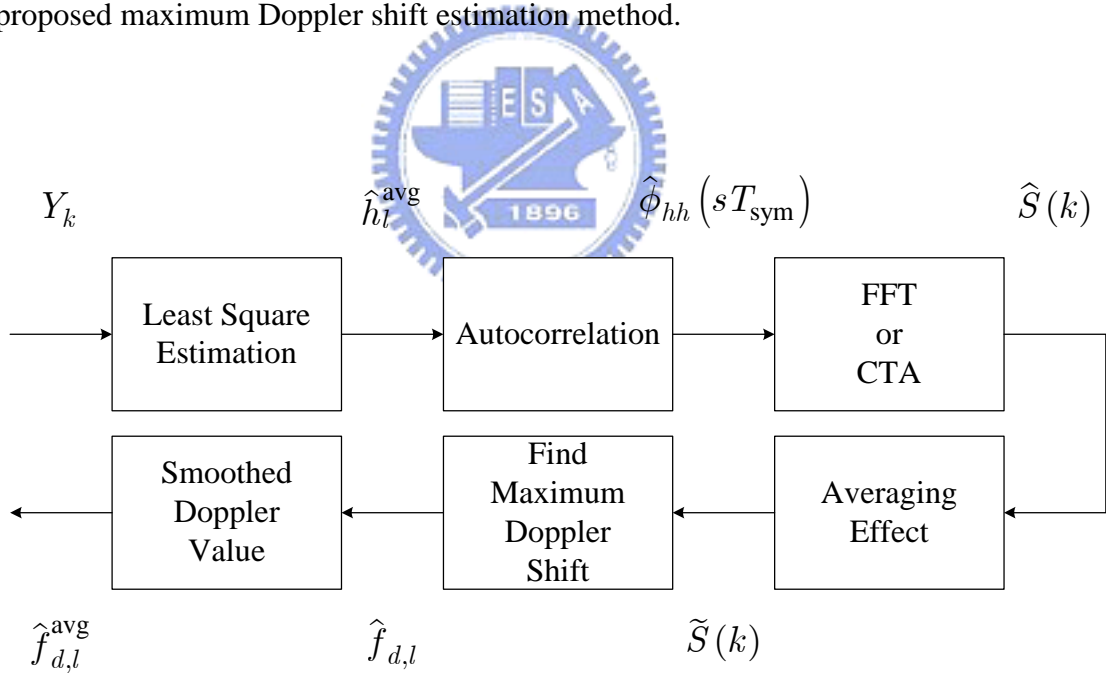
Figure 3.4: Block diagram of proposed Doppler shift estimation method

Here, we utilize frequency domain scattered pilot tones [1], [21] of DVB-T systems to estimate channel response. Therefore, let $L \leq N_P$ be the maximum predicted normalized length of channel. Then, the $N_P \geq (L+1)$ equally spaced pilots,

P_{k_p}, are inserted at subcarriers k_p for $0 \leq p \leq (N_P - 1)$. Form Equation (3.9), a least square (LS) estimation of the channel transfer function at the pilot subcarriers can be obtained as

$$\widehat{H}_{k_p} = \frac{Y_{k_p}}{P_{k_p}} = H_{k_p} + \frac{\left(I_{k_p} + V_{k_p}\right)}{P_{k_p}}, \; 0 \leq p \leq (N_P - 1). \qquad (3.15)$$

In Equation (3.15), I_{k_p} and V_{k_p} denotes ICI term and noise term at k_p-th subcaeeier, respectively. Then, through an N_P-point IFFT, the estimated CIR $\hat{h}_l^{\text{avg}}$ would be

$$\hat{h}_l^{\text{avg}} = \frac{1}{N_P} \sum_{p=0}^{N_P - 1} \widehat{H}_{k_p} e^{j2\pi pl / N_P}, \; 0 \leq l \leq (N_P - 1). \qquad (3.16)$$

In this thesis, we approximate channel time-variations with a piece-wise linear model during one symbol period T_{sym}. In Figure 3.5, the solid curve is real or imaginary part of a channel path, and the dashed line is piece-wise linear model. By the assumption above, $E\left(\left|h_l^{\text{avg}} - h_{n,l}\right|\right)$ is minimized at $n = (N/2 - 1)$ for the l-th channel tap [22]. We approximate $h_{(N/2-1),l}$ with the estimate of h_l^{avg}. Thus, we will have

$$\hat{h}_{\left(\frac{N}{2}-1\right),l} = \hat{h}_l^{\text{avg}} \qquad (3.17)$$
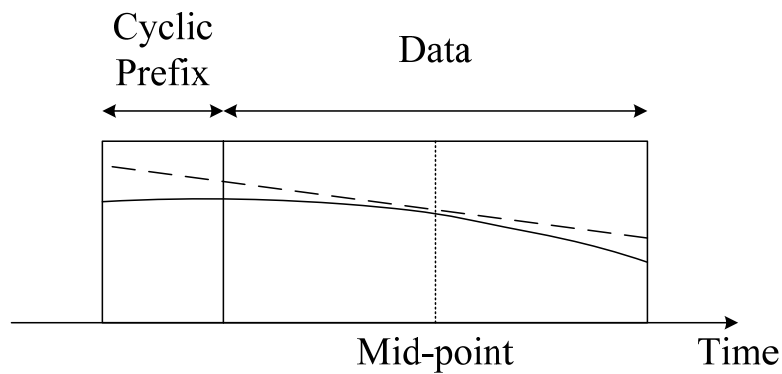
Figure 3.5: Piece-wise linear model in one OFDM symbol period

From Equation (3.13) and Equation (3.17), the estimated ACF of the channel impulse response of l-th tap can be expressed as

$$\hat{\phi}_{hh}\left(s \cdot T_{\text{sym}}\right) = E\left\{\hat{h}_{\left(\frac{N}{2}-1\right),l} \cdot \hat{h}^*_{\left(\frac{N}{2}-1+s \cdot T_{\text{sym}}\right),l}\right\}$$

$$= J_0\left(2\pi f_{d,l} \cdot s \cdot T_{\text{sym}}\right) + \sigma_\Delta^2 \cdot \delta\left(\tau_l\right)$$

$$= \phi_{hh}\left(s \cdot T_{\text{sym}}\right) + \sigma_\Delta^2 \cdot \delta\left(\tau_l\right), \tag{3.18}$$

where s is the difference in OFDM symbol index, T_{sym} denotes the symbol period, and σ_Δ^2 is the combined reduced variance of ICI plus AWGN. Here, the estimated Doppler power spectrum over an observation interval of K symbols can be written as

$$\hat{S}_K\left(k\right) = \text{FT}\left\{\hat{\phi}_{hh}\left(s \cdot T_{\text{sym}}\right)\right\}$$

$$= \sum_{s=0}^{K-1} \hat{\phi}_{hh}\left(s \cdot T_{\text{sym}}\right) e^{-j2\pi ks/K}, \quad 0 \le k \le (K-1). \tag{3.19}$$

If the Doppler power spectrum is approximated over sufficient many observation intervals, the maximum Doppler shift can be estimated by finding the maximum peak of the estimated Doppler power spectrum series. However, excessively long length of observation would lead to an estimation delay and a degradation of the Doppler shift tracking ability.

From Figure 3.3, we can know that the maximum peak of the Doppler power spectrum locates within a small frequency domain interval. Thus, in order to increase the accuracy of maximum Doppler shift estimation, the zero-padding would be used. The K-sample estimated ACF sequence (Equation 3.18) is extended to a K_{FFT}-sample sequence by padding with $\left(K_{\text{FFT}} - K\right)$ zero samples. Therefore, we obtain

$$\hat{\mathbf{S}}_{K_{\text{FFT}}} = \text{FFT}\left\{\left[\hat{\phi}_{hh}\left(0\right), \hat{\phi}_{hh}\left(T_{\text{sym}}\right), \cdots, \hat{\phi}_{hh}\left((K-1) \cdot T_{\text{sym}}\right), 0, 0, \cdots, 0\right]\right\} \tag{3.20}$$

However, we only need a particular small frequency domain interval for Doppler shift estimation. Thus, we introduce the chirp transform algorithm [23] to provide another alternative choice for Fourier transform.

3.2.1 Chirp Transform Algorithm (CTA)

Unlike the FFT scheme, the CTA scheme [22] can be used to compute any set of equally spaced samples of the Fourier transform, thus the CTA scheme is more flexible than the FFT scheme. From Equation (3.19), we denote that

$$\widehat{\Phi}_K = \left[\hat{\phi}_{hh}(0), \hat{\phi}_{hh}(T_{\mathrm{sym}}), \cdots, \hat{\phi}_{hh}((K-1) \cdot T_{\mathrm{sym}}) \right] \tag{3.21}$$

as a K-point sequence and $\widehat{\mathbf{S}}_K$ is its Fourier transform. Consider the evaluation of M samples of $\widehat{\mathbf{S}}_K$ that are equally spaced in angle on the unit circle at frequencies

$$w_k = w_0 + k\Delta w, \tag{3.22}$$

where w_0 is the start frequency and the frequency increment Δw can be chosen arbitrarily. Figure 3.6 shows the frequency samples for the CTA scheme.
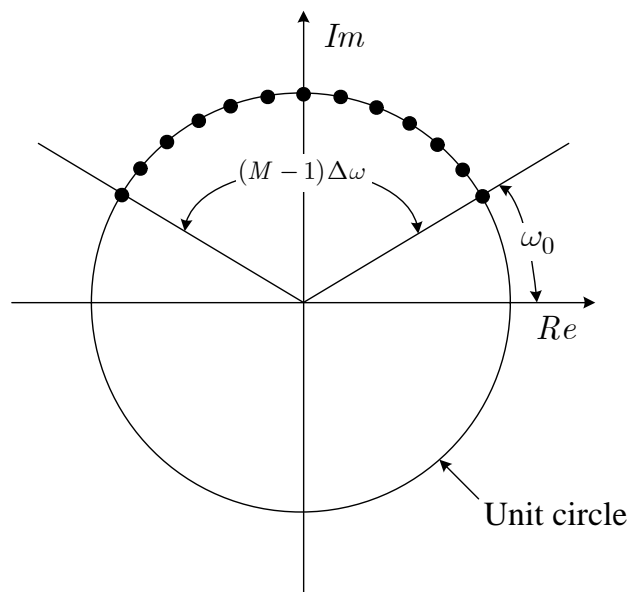
Figure 3.6: Frequency samples for chirp transform algorithm

The Fourier transform corresponding to the more general set of frequency samples can be written as

$$\widehat{S}_M(k) = \sum_{n=0}^{K-1} \widehat{\Phi}_K(n) e^{jw_k n}, \ k = 0,1,\cdots,(M-1).$$ (3.23)

Then, substituting Equation (3.22) into Equation (3.23) can obtain

$$\widehat{S}_M(k) = \sum_{n=0}^{K-1} \widehat{\Phi}_K(n) e^{jw_0 n} W^{nk},$$ (3.24)

where W defined as

$$W = e^{-j\Delta w}.$$ (3.25)

Here, we use the identity

$$nk = \frac{1}{2}\left[n^2 + k^2 - (k-n)^2\right]$$ (3.26)

to express Equation (3.24) as

$$\widehat{S}_M(k) = W^{\frac{w^2}{2}}\left[\sum_{n=0}^{K-1} g(n) W^{-\frac{(k-n)^2}{2}}\right], \ k = 0,1,\cdots,(M-1),$$ (3.27)

where $g(n)$ defined as

$$g(n) = \widehat{\Phi}_K(n) e^{jw_0 n} W^{\frac{n^2}{2}}.$$ (3.28)

However, we need only compute the output of the system in Figure 3.7 over a finite interval for the evaluation of the Fourier transform samples specified in Equation (3.27).

$$
\Phi_K(n) \xrightarrow{\quad} \otimes \xrightarrow{\quad g(n)\quad} \boxed{\begin{array}{c} \text{FIR chirp filter} \\ h(n)=W^{-\frac{n^2}{2}} \end{array}} \xrightarrow{\quad} \otimes \xrightarrow{\quad \widehat{S}_M(n)}
$$

$$
e^{-jw_0 n}W^{\frac{n^2}{2}} \qquad\qquad W^{\frac{n^2}{2}}
$$
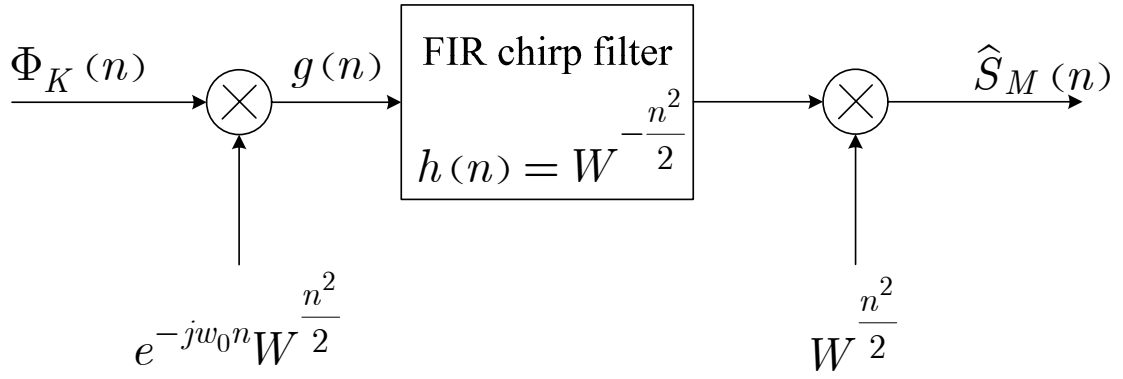
Figure 3.7: Block diagram of chirp transform algorithm

Since $g(n)$ is finite duration, only a finite portion of the sequence $W^{-n^2/2}$ is used in obtaining $g(n)*W^{-n^2/2}$ over the interval $0 \le n \le (M-1)$. Let us define

$$
h(n) = \begin{cases} W^{-\frac{n^2}{2}}, & -(N-1) \le n \le (M-1), \\ 0, & \text{otherwise,} \end{cases} \tag{3.29}
$$

so we have

$$
g(n)*W^{-\frac{n^2}{2}} = g(n)*h(n), \ n=0,1,\cdots,(M-1). \tag{3.30}
$$

However, in Equation (3.29) $h(n)$ is noncausal, and for certain real-time implementation it must be modified to obtain a causal system. Therefore, this modification is easily accomplished by delaying $h(n)$ by $(N-1)$ to obtain a causal impulse response:

$$
h_{\mathrm{c}}(n) = \begin{cases} W^{-\frac{(n-N+1)^2}{2}}, & 0 \le n \le (M+N-2), \\ 0, & \text{otherwise.} \end{cases} \tag{3.31}
$$

Since both the chirp demodulation factor at the output and the output signal are also delayed by $(N-1)$ samples, the results of the CTA scheme are

$$
\widehat{S}_M(k) = G(n+N-1), \ n=0,1,\cdots,(M-1). \tag{3.32}
$$

By modifying the system of Figure 3.7, we can obtain a causal system as shown in Figure 3.8.
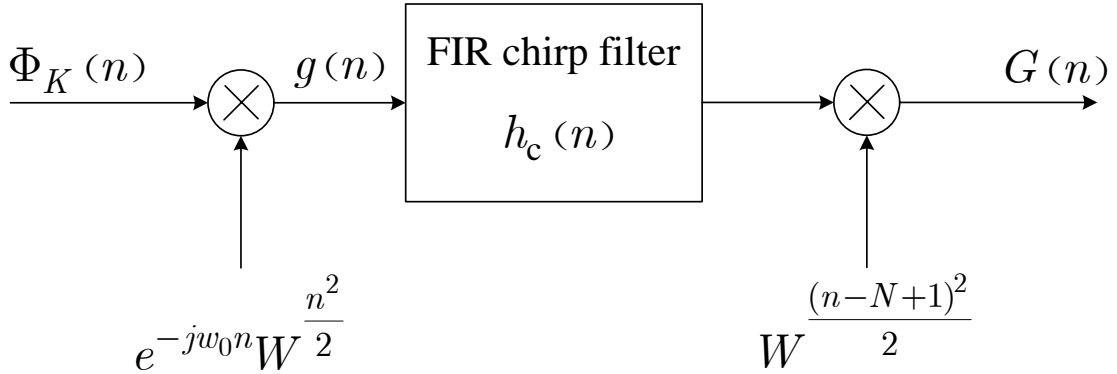
Figure 3.8: Block diagram of chirp transform algorithm for causal finite-length impulse response

3.2.2 Averaging and Smoothing Effect of Maximum Doppler Shift Estimation Method

If the observation interval with K symbols is not long enough, the Doppler information does not have a sufficient statistical characteristic on the estimated Doppler power spectrum $\hat{S}_M(k)$. Therefore, the proposed maximum Doppler shift estimation is overlapped every $K/2$ samples to deal with this problem, as shown in Figure 3.9. As the estimated Doppler power spectrum is accumulated, the variance of the noise and the interference power spectrums can be reduced over whole spectrum range and the estimated maximum Doppler shift would become more accuracy.
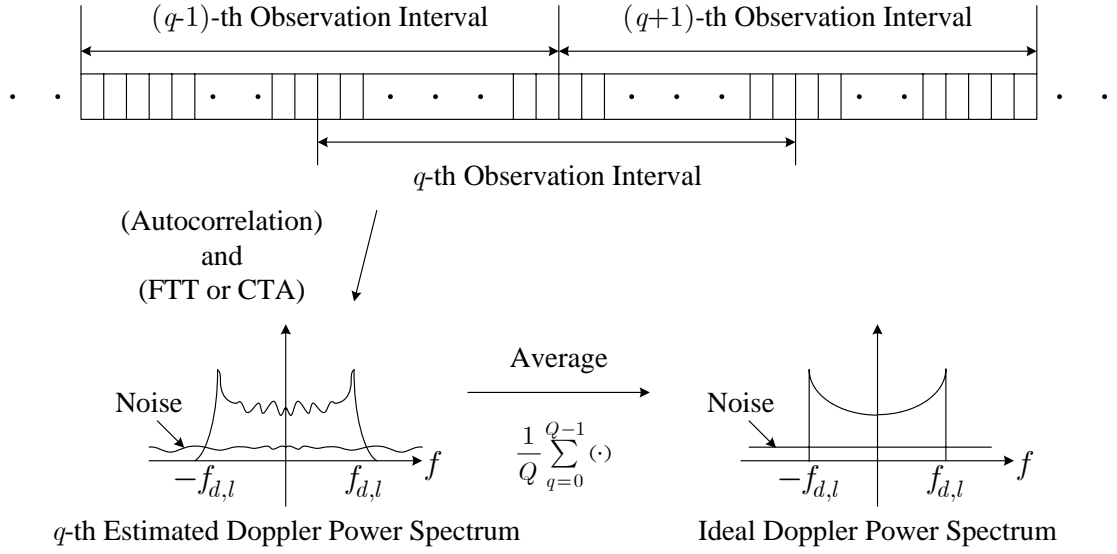
Figure 3.9: Averaging effect of estimated Doppler power spectrum

If the Doppler shift does not change during Q times of observation interval, the ideal Doppler power spectrum can be approximated by averaging Q times of the estimated Doppler power spectrum. Thus, we obtain

$$\widetilde{S}_M(k) = \frac{1}{Q} \sum_{q=0}^{Q-1} \widehat{S}_M^{(q)}(k), \ k = 0, 1, \cdots, (M-1), \tag{3.33}$$

where $\widehat{S}_M^{(q)}(k)$ denotes the q-th estimated Doppler power spectrum. Then, the estimated maximum Doppler shift can be obtained as

$$\widehat{f}_{d,l} = \frac{w_{M-1} - w_0}{2\pi M} \cdot \left(\underset{k}{\arg\max} \, \widetilde{S}_M(k) \right), \ 0 \le k \le M-1. \tag{3.34}$$

The Doppler shift estimation above described provides an instantaneous estimated of Doppler shift over Q times of observation interval. The smoothed Doppler spread values over a long period of time can be calculated as [7], [10]

$$\widehat{f}_{d,l}^{avg}(n) = \left(1 - \beta(\Delta f)\right) \cdot \widehat{f}_{d,l}(n) + \beta(\Delta f) \cdot \widehat{f}_{d,l}^{avg}(n-1). \tag{3.35}$$

Here, the absolute difference Δf between the current estimated and the previous

smoothed estimate can be written as

$$\Delta f = \left| \hat{f}_{d,l}(n) - \hat{f}_{d,l}^{avg}(n-1) \right|, \tag{3.36}$$

and the smoothing factor $0 < \beta(\Delta f) < 1$ that determines the tracking ability is expressed as

$$\beta(\Delta f) = \begin{cases} 1, & \Delta f > \Delta f_{\max}, \\ \dfrac{\Delta f}{\Delta f_{\max}}, & \Delta f \leq \Delta f_{\max}. \end{cases} \tag{3.37}$$

$\Delta f_{\max}$ is a maximum frequency difference. Note that $\Delta f_{\max}$ depends on update period.

3.3 Complexity Analyses of FFT and CTA

In this section, the computational complexity and the memory size requirement of the FFT and the CTA schemes are compared. Here, we denote the number of arithmetic multiplications and additions as a measure of computational complexity. First, we consider the complexity analysis of the CTA scheme. From Figure 3.8, the input part of CTA needs K complex multiplications. Then, the computation of each result of convolution requires K complex multiplications and K complex additions, and the output part of CTA needs M complex multiplications. Therefore, the total computation of the CTA scheme requires $(M+1) \cdot K + M$ complex multiplications and $M \cdot K$ complex additions. In the CTA scheme, the input part and output part require one complex memory respectively; the convolution part needs $(K + M - 1)$ complex memories. Thus, the total memory size of the CTA scheme requires $(K + M + 1)$ complex memories. Next, we consider FFT scheme. A K_{FFT}-point FFT needs $(K_{\text{FFT}} / 2) \cdot (\log_2 K_{\text{FFT}})$ complex multiplications and $K_{\text{FFT}} \cdot (\log_2 K_{\text{FFT}})$ complex

additions. Moreover, the FFT scheme needs K_{FFT} complex memories for input storage and K_{FFT} complex memories for output storage. The total memory size of the FFT scheme requires $2 \cdot K_{\text{FFT}}$ complex memories for a general case. Here, Table 3.2 lists the above results.

Table 3.2: Complexity analysis of CTA and FFT

	CTA scheme	FFT scheme
Computation	Complex multiplications: $(M+1) \cdot K + M$	Complex multiplications: $(K_{\text{FFT}} / 2) \cdot (\log_2 K_{\text{FFT}})$
	Complex additions: $M \cdot K$	Complex additions: $K_{\text{FFT}} \cdot (\log_2 K_{\text{FFT}})$
Memory size	Complex memories: $(K + M + 1)$	Complex memories: $2 \cdot K_{\text{FFT}}$

Then, we will give some examples to experience complexity. First, we know that the CTA scheme has K-sample input and the M-sample output. The observation interval K is 64, 128, or 256 symbols. The CTA scheme can estimate the maximum Doppler shift during 0 Hz to 300 Hz, and the frequency domain resolution of CTA is set equal to or less than 1 Hz per sample. As the result, the number of CTA output, M, must be equal to or greater than 300. When both of the CTA and the FFT schemes have the same frequency domain resolution, the parameter K_{FFT} of FFT scheme should be satisfy

$$\log_2 (K_{\text{FFT}}) = \text{nextpow2} \left(\frac{1}{T_{\text{sym}}} \right), \tag{3.38}$$

where nextpow2($\cdot$) is the next higher power of 2. Moreover, the symbol duration, T_{sym}, for DVB-T systems is listed in Table 3.3. Therefore, the values of K_{FFT} are between 1024 and 8192.

Table 3.3: Symbol duration for DVB-T systems

	2K mode	8K mode
6 MHz channels	308 μs (min.) 373.33 μs (max.)	1232 μs (min.) 1493.33 μs (max.)
7 MHz channels	264 μs (min.) 320 μs (max.)	1056 μs (min.) 1280 μs (max.)
8 MHz channels	231 μs (min.) 280 μs (max.)	924 μs (min.) 1120 μs (max.)

According to the above parameters, the minimum computational complexity of the CTA scheme is 17,614 complex multiplications and 17,280 complex additions; the maximum computational complexity is 69,646 complex multiplications and 69,120 complex additions. The minimum computational complexity of the FFT scheme is 5,120 complex multiplications and 10,240 complex additions; the maximum computational complexity is 53,248 complex multiplications and 106,496 complex additions. In the CTA scheme, the minimum and maximum number of memory is 335 and 527 complex memories, respectively. In the FFT scheme, the minimum and maximum number of memory is 2,048 and 16,384 complex memories, respectively. Therefore, the FFT scheme has less computational complexity than the CTA scheme, but the FFT scheme needs the larger memory size of the CTA scheme. When the memory size is the more important consideration factor, the CTA scheme is a better choice.

3.4 Computer Simulations

In this section, simulation results of the proposed maximum Doppler shift estimation will be presented. Through out the all simulations, timing synchronization is assumed to be perfect. Simulation parameters are summarized in Table 3.4. Consider a 2048-subcarrier (which is the 2K mode of DVB-T systems) OFDM system with bandwidth 6 MHz. Transmitted data sequences are modulated in QPSK constellation, and Jakes model is used as the channel model. The maximum Doppler shift in the simulation varies form 0 Hz to 300 Hz. As the mobile velocity is 456 km/hour in the carrier frequency 710 MHz case, the corresponding maximum Doppler shift is 300 Hz. Thus the maximum Doppler shift that we simulated is limited to 300 Hz. The CTA scheme is used and the frequency domain resolution is 1 Hz. The maximum frequency difference $\Delta f_{\max}$ is 50 Hz.
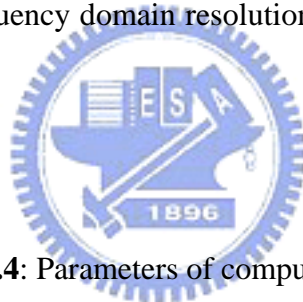
Table 3.4: Parameters of computer simulations

System	DVB-T
Transmission mode	2K
Channel bandwidth	6 MHz
CP length	1/4 OFDM symbol
Modulation	QPSK
Carrier frequency	710 MHz
Maximum Doppler shift	0 ~ 300 Hz
Channel model	Jakes model

Figure 3.10 shows the simulation results for the effect of the accumulation size Q when the observation interval K equals to 128. It is shown that the large Q size can be sufficiently estimated low SNR (< 10 dB). If the accumulation size is larger than 5 times, the normalized mean square error (MSE) of proposed method does not reduce obviously. The normalized MSE denote as

$$\text{normailzed MSE} = E\left\{\left|\frac{\hat{f}_d - f_d^{\text{ideal}}}{f_d^{\text{ideal}}}\right|^2\right\}. \tag{3.39}$$

Therefore, the 7 times accumulation size is sufficient for observation 128 symbols. The error floor is due to the imperfect Doppler power spectrum.
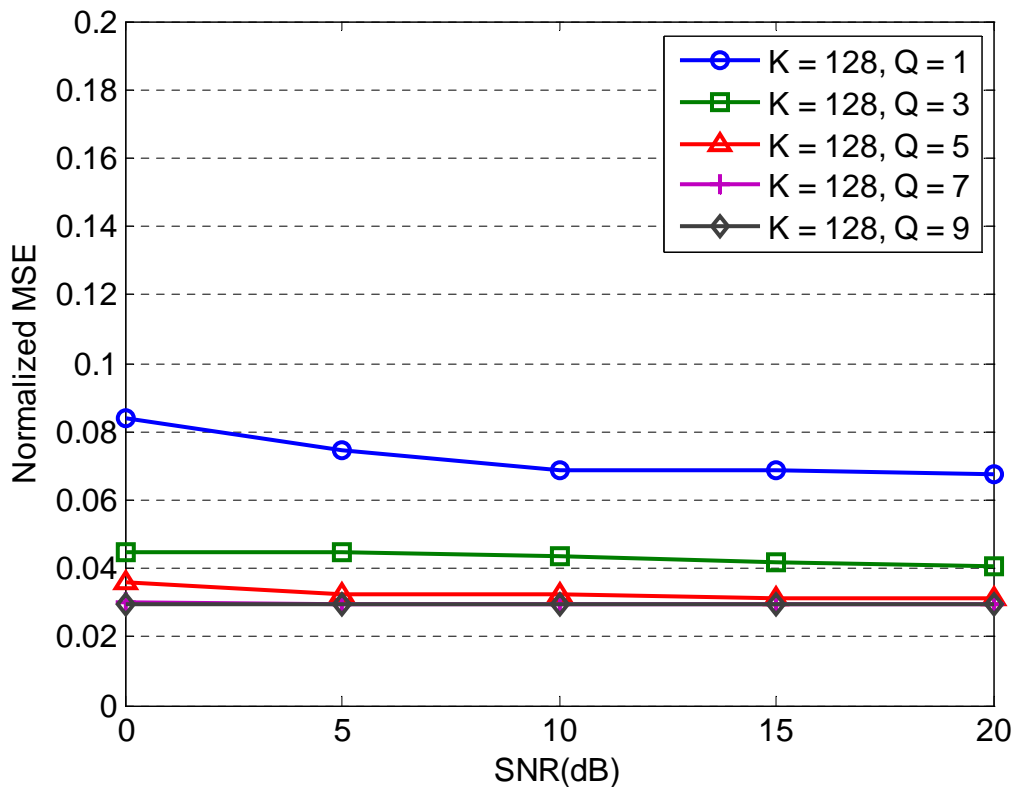

Figure 3.10: Normalized MSE versus SNR. The effect of different accumulation size Q is shown. The observation interval K is 128 symbols and the maximum Doppler shift is 0 Hz to 300 Hz.

Figure 3.11 shows the normalized MSE of estimation error versus accumulation size for various observation intervals in SNR = 15 dB. When the observation interval and accumulation size become larger, the estimated Doppler power spectrum becomes closer to the ideal Doppler power spectrum, thus the estimated value is more accuracy, as shown in Figure 3.11. However, the long observation intervals and the large accumulation size will increase the estimation delay and the computational complexity. Therefore, the various observation intervals and the accumulation size should be chosen carefully by taking the accuracy, estimation delay, and computational complexity into consideration. From Figure 3.11, we can see that when the observation interval equals to 256 or 128 symbols, $Q = 5$ is sufficient, and when the observation interval equals to 64 symbols, $Q = 7$ is sufficient.
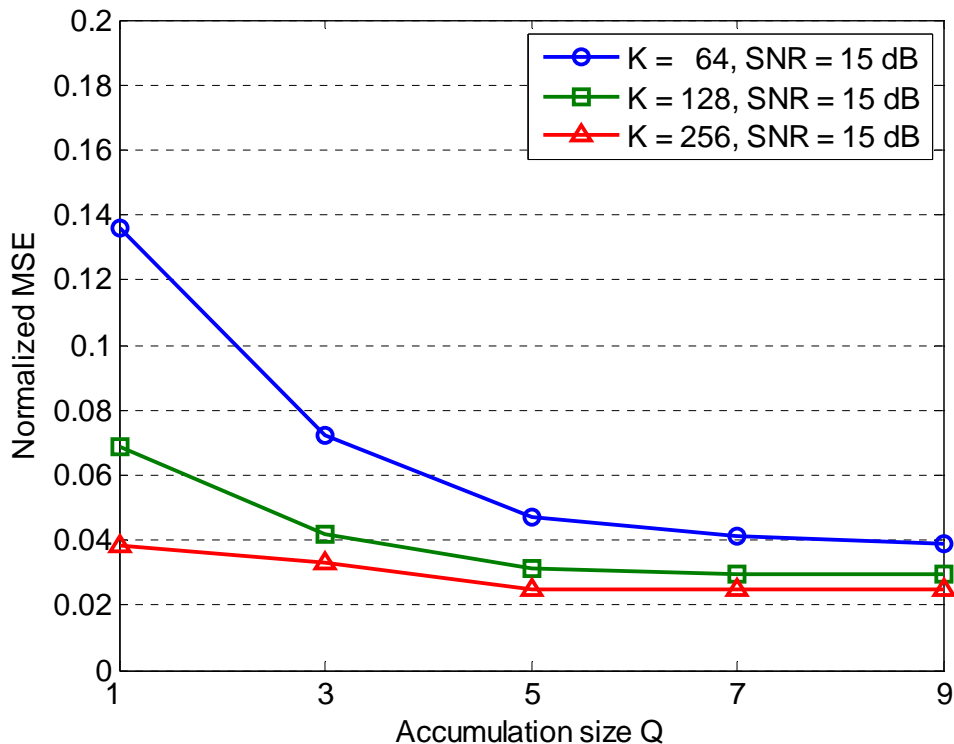

Figure 3.11: Normalized MSE versus accumulation size. The effect of different observation interval K is shown. The maximum Doppler shift is 0 Hz to 300 Hz and SNR is 15 dB.

The simulation results of the normalized MSE for different observation interval and SNR versus accumulation size are presented in Figure 3.12. As the SNR becomes larger, the estimated CIRs are more accurate. When estimated CIRs are more accurate, the estimated Doppler power spectrum would also become more accurate. Because the accuracy of the estimated Doppler power spectrum is greatly influenced by the observation interval and the accumulation size, these two parameters are main factors in the estimation scheme. When the Q is larger than 5, the proposed method has a stable performance. Figure 3.13 to Figure 3.15 show the tracking ability of the proposed maximum Doppler shift estimation method. The estimated and the actual Doppler spread profiles are both listed in these figures. As the result, the proposed method tracks well for Doppler shift changes, even though the SNR is low than 10 dB.
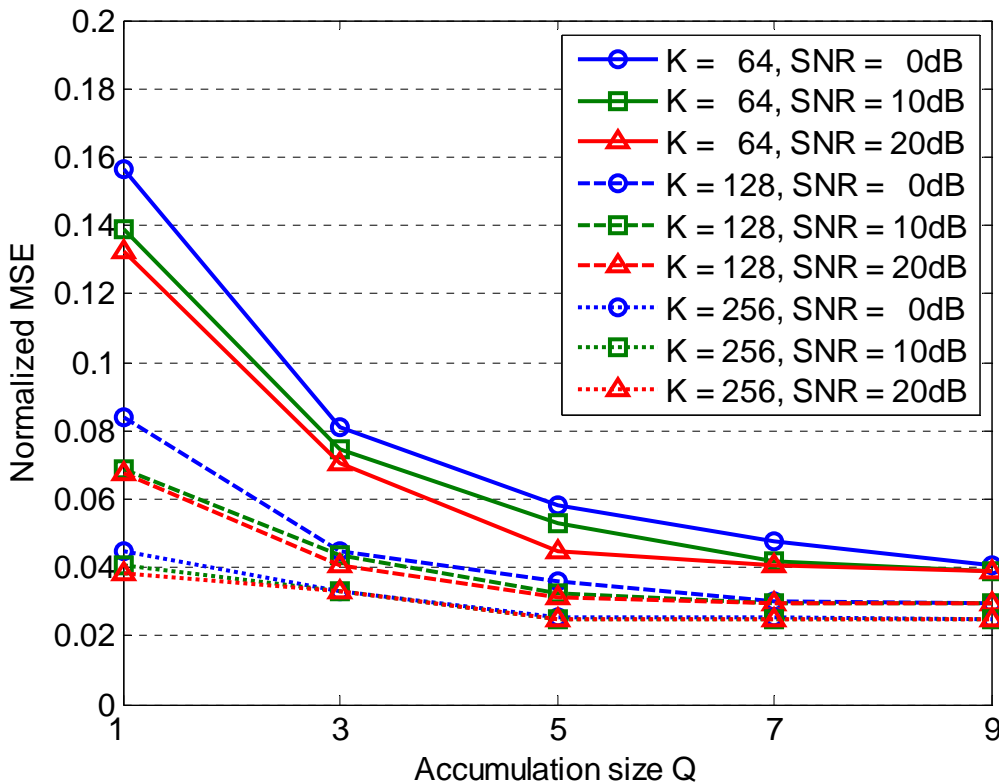
Figure 3.12: Normalized MSE versus accumulation size for different observation intervals and SNR. The maximum Doppler shift is 0 Hz to 300 Hz.
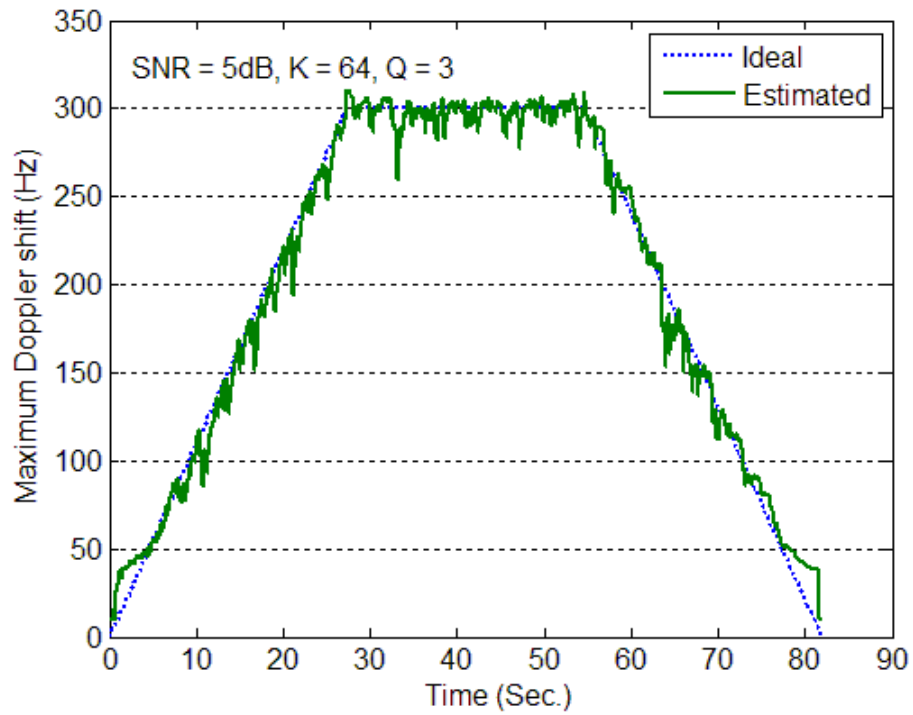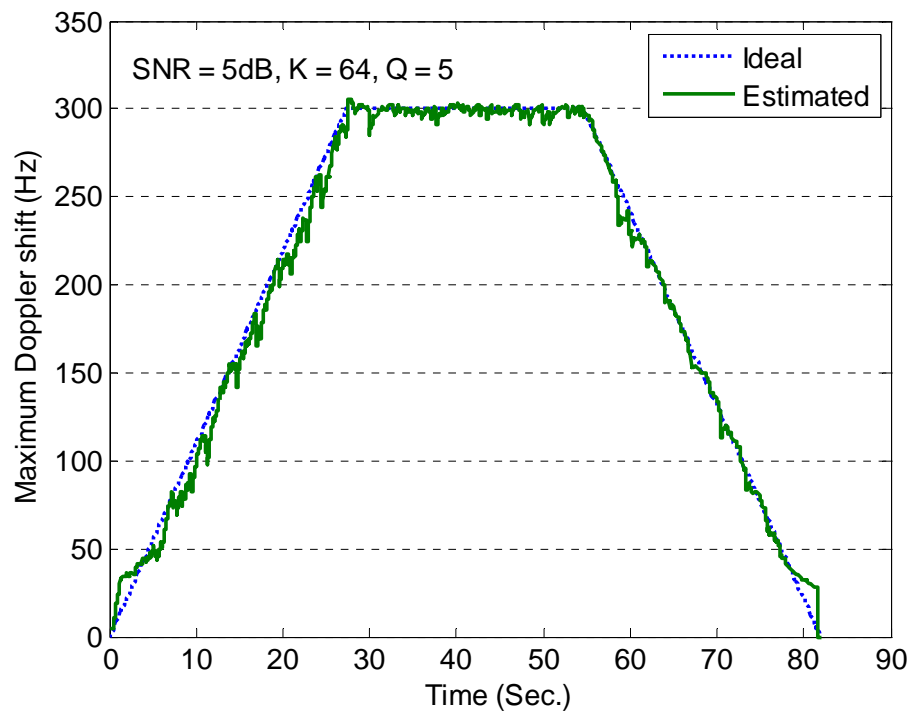
Figure 3.13: Tracking ability of the proposed maximum Doppler shift estimation method for SNR = 5dB. (a) $K = 64$ with $Q = 3$. (b) $K = 64$ with $Q = 5$.
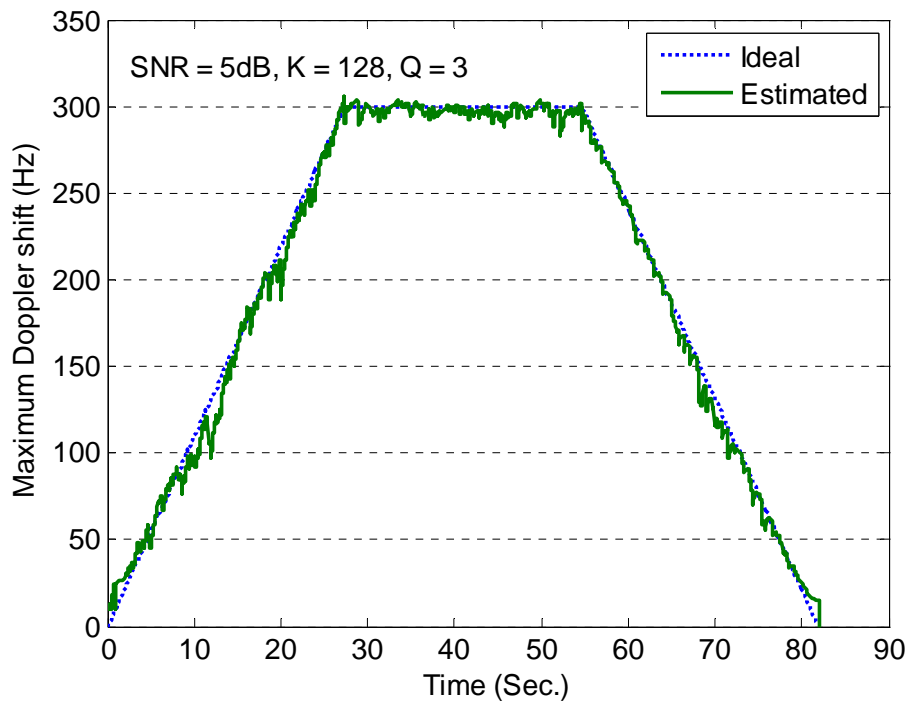
(a)
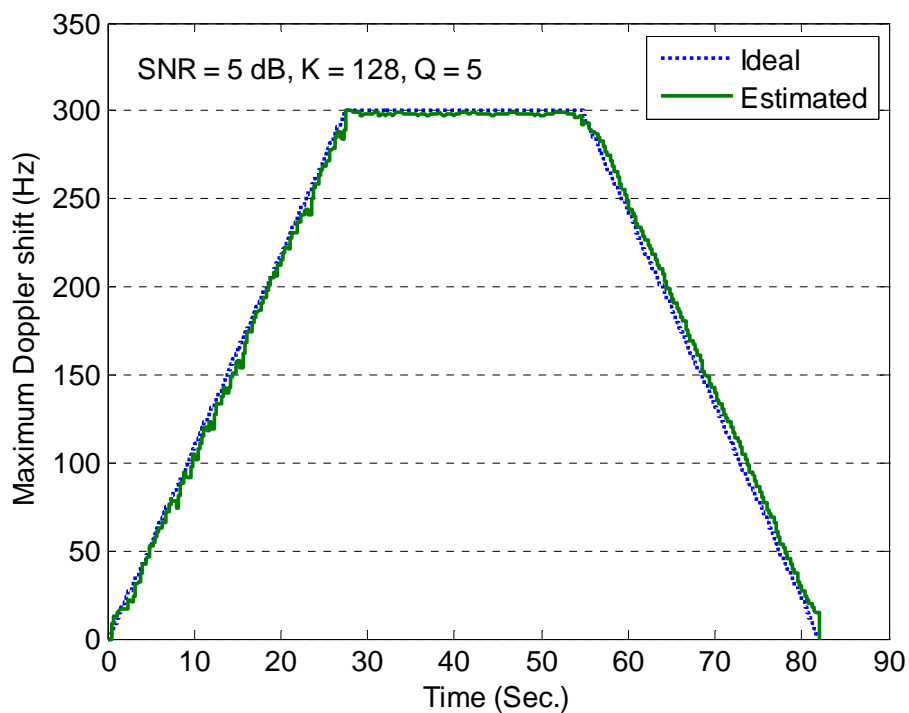
(b)

Figure 3.14: Tracking ability of the proposed maximum Doppler shift estimation method for SNR = 5dB. (a) $K = 128$ with $Q = 3$. (b) $K = 128$ with $Q = 5$.
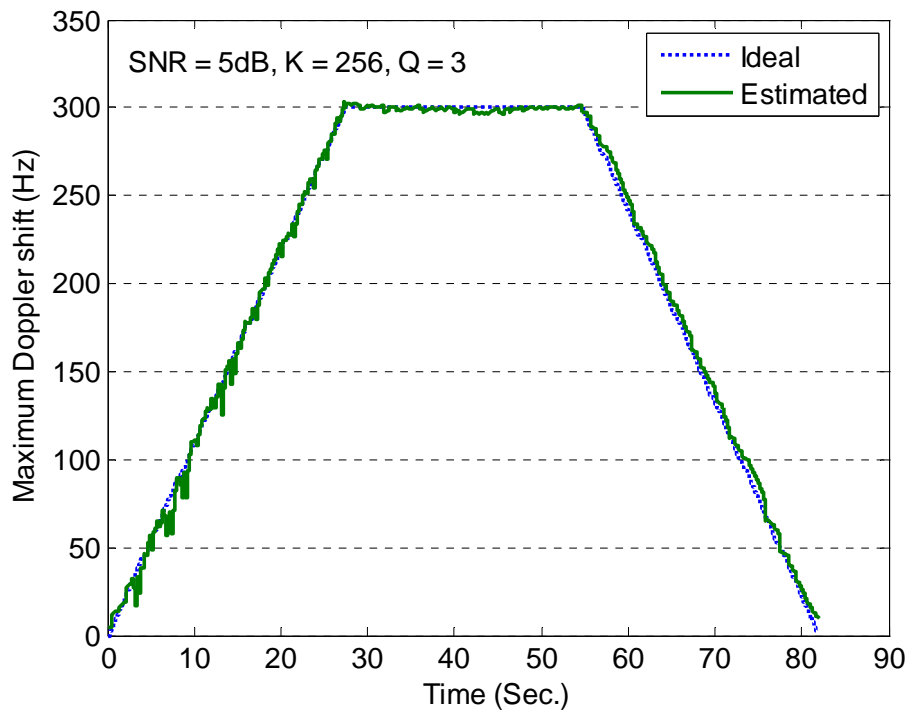
(a)
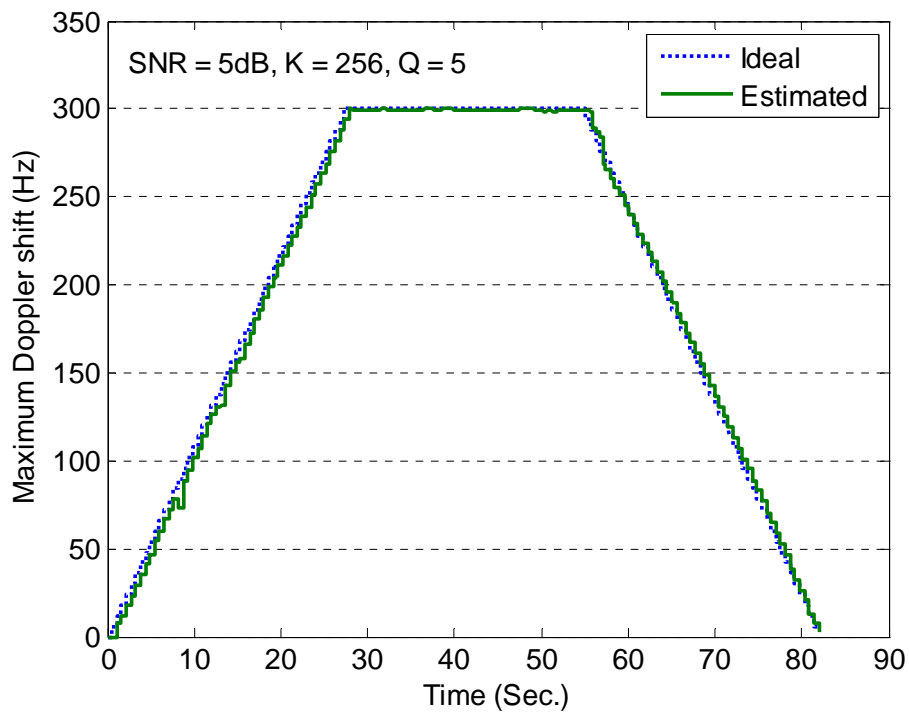
(b)

Figure 3.15: Tracking ability of the proposed maximum Doppler shift estimation

method for SNR = 5dB. (a) $K = 256$ with $Q = 3$. (b) $K = 128$ with $Q = 5$.

Figure 3.15 shows three paths with different maximum Doppler shifts. The maximum Doppler shift of path I varies from 0 to 300 Hz. The maximum Doppler shift of path II varies from 300 to 60 Hz. The maximum Doppler shift of path III varies from 0 to 145 Hz. As can be seen, the proposed method (with $K = 256$ and $Q = 5$) still tracks well in SNR = 5dB. Figure 3.16 shows the comparison between Park's method [10] and the proposed method in SNR = 15 dB. The error flow of Park's method is owing to the limit of FFT spectrum resolution. The proposed method has a superior frequency domain resolution of Doppler power spectrum, but the computational complexity is larger than the computational complexity in Park's method.
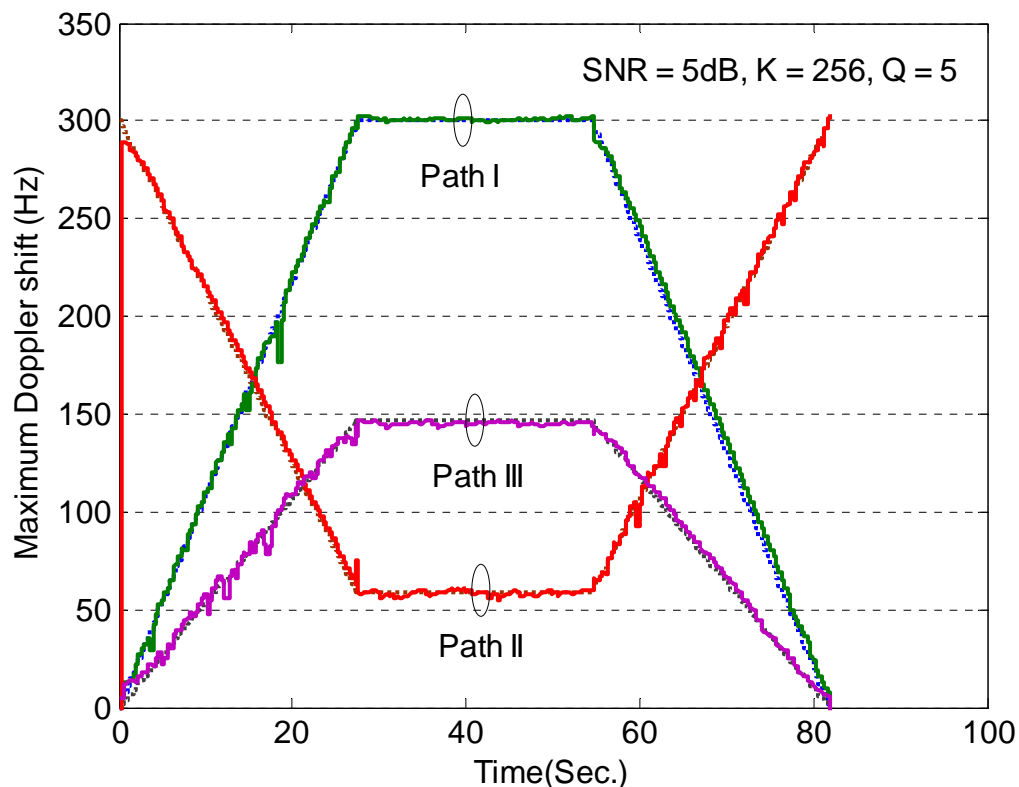
Figure 3.15: Tracking ability of the proposed maximum Doppler shift estimation method for three paths. ($K = 256$, $Q = 5$, and SNR = 5 dB)
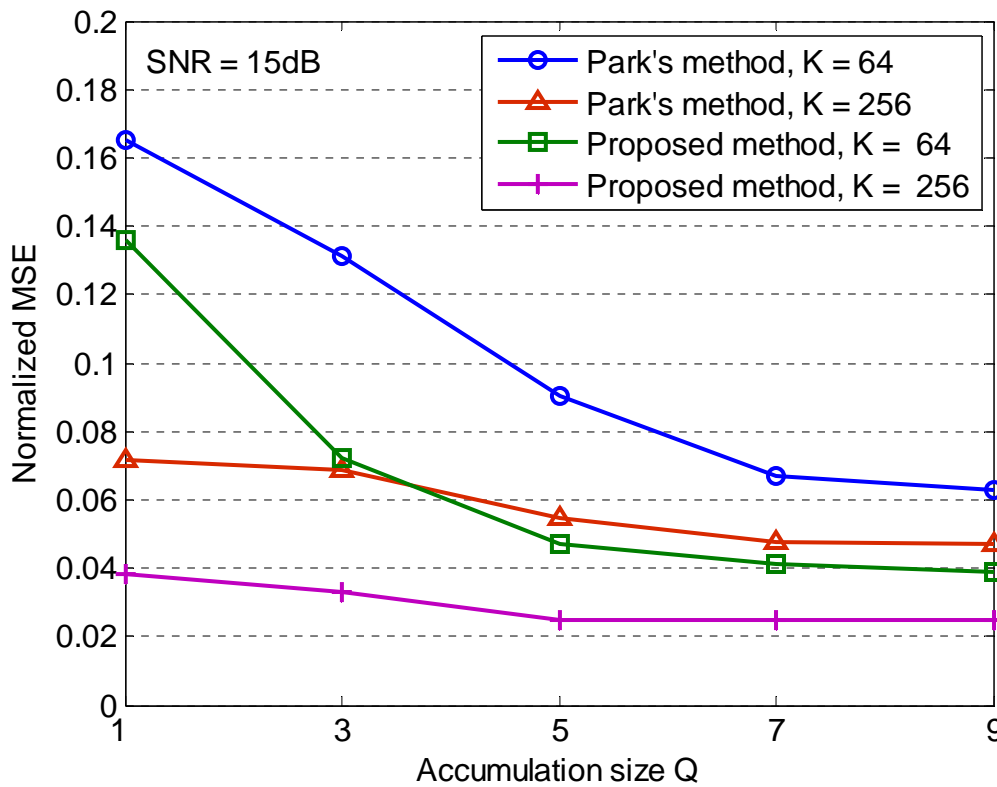
Figure 3.16: Normalized MSE versus accumulation size. Compared Park's method [10] with proposed method (SNR = 15 dB).

3.5 Summary

In this chapter, a maximum Doppler shift estimation method using Doppler power spectrum is proposed. It is shown that the proposed method works well over wide Doppler shift at low SNR condition ($<$ 10 dB). This method provides a tradeoff between computational complexity and estimation accuracy by changing the size of observation interval and accumulation. Furthermore, two schemes of Fourier transform (FFT scheme and CTA scheme) are proposed to provide a tradeoff between computational complexity and the memory size. The FFT scheme has lower computational complexity than the CTA scheme, but it needs larger memory size than the CTA scheme.

Chapter 4

ICI Cancellation in OFDM Systems over Time-Varying Channels

In this chapter, we propose an adaptive ICI cancellation scheme based on [5]. The proposed method provides a tradeoff between the performance of output signals and processing time. Through the ICI analysis, the relation between ICI and the maximum Doppler shift will be introduced. Then, from Chapter 3, we can utilize the estimated maximum Doppler shift as a parameter of the adaptive ICI cancellation scheme.

First, Section 4.1 presents the ICI analysis. In Section 4.2, the proposed adaptive ICI cancellation scheme is described. The computer simulations and the summary are shown in Section 4.3 and Section 4.4, respectively.

4.1 ICI Analysis

Signals transmitted in a mobile environment are often impaired by the delay spread and Doppler shift. In order to keep a near-constant channel in each subcarrier of OFDM systems, the length of an OFDM symbol should be increase as the delay spread increases. Since the delay spread increased, the length of the guard interval should also be expanded to prevent the ISI. However, because of the symbol duration increased, the

OFDM system became sensitive to time-varying channels. The orthogonality between subcarriers is lost in time-varying channels, resulting in intercarrier interference (ICI), which stains the optimal data detection, and degrades the bit-error-rate (BER) performance in OFDM systems.

From Equation (3.9), the k-th subcarrier signal after the FFT at the receiver side can be rewritten as

$$Y_k = H_k X_k + I_k + W_k, \ 0 \leq k \leq N - 1 \tag{4.1}$$

In Equation (4.1), the ICI term, I_k, is caused by the time-varying channel. In a time-invariant channel, the I_k is zero and $E\{|H_k|^2\} = 1$. In a slow time-varying channel (i.e., the normalized maximum Doppler shift is small), the ICI power can be assumed as $E\{|I_k|^2\} \approx 0$. Here, the normalized maximum Doppler shift, f_n, is denoted the maximum Doppler shift normalized to the OFDM symbol duration ($N \cdot T_s$). If f_n is small, the ICI power can be neglected compared to the background noise power [24]. On the other hand, when the normalized maximum Doppler shift is high, the ICI effects are too critical to be ignored. In addition, the power of the desired signal spreads out to neighboring subcarriers, because of $E\{|H_k|^2\} < 1$.

4.1.1 ICI in OFDM Systems

Here, an OFDM system model over time-varying channels is considered. Form Equation (3.3), the channel is modeled by the time-varying discrete impulse response, $h(n,l)$, which is defined as the response of time n to an impulse response applied at l-th tap. After transmitting through the channel, the received sample sequences which are the convolution results between transmitted symbols and time-varying channels.

Therefore, Equation (3.5) can be expressed in a matrix form:

$$
\begin{bmatrix} y_0 \\ y_1 \\ \vdots \\ y_{N-1} \end{bmatrix} = \begin{bmatrix} h_{0,0} & 0 & \cdots & 0 & h_{0,L-1} & \cdots & h_{0,1} \\ h_{1,1} & h_{1,0} & 0 & \cdots & 0 & h_{1,L-1} & \cdots \\ \vdots & h_{2,1} & h_{2,0} & 0 & \cdots & 0 & h_{2,L-1} \\ h_{(L-1),(L-1)} & \vdots & \ddots & \ddots & 0 & \cdots & 0 \\ 0 & h_{L,(L-1)} & \cdots & \cdots & h_{L,0} & 0 & \vdots \\ \vdots & 0 & \ddots & \ddots & \ddots & \ddots & 0 \\ 0 & \cdots & 0 & h_{(N-1),(L-1)} & \cdots & \cdots & h_{(N-1),0} \end{bmatrix} \cdot \begin{bmatrix} x_0 \\ x_1 \\ \vdots \\ x_{N-1} \end{bmatrix}
$$

$$
+ \begin{bmatrix} \nu_0 \\ \nu_1 \\ \vdots \\ \nu_{N-1} \end{bmatrix}. \tag{4.2}
$$

In Equation (4.2), $h_{n,l}$ represents the channel response of the l-th tap at the time instance n. Then, the above equation can be rewritten as

$$
\vec{\mathbf{y}} = \mathbf{H}_{\mathrm{TD}} \cdot \vec{\mathbf{x}} + \vec{\nu}, \tag{4.3}
$$

where $\mathbf{H}_{\mathrm{TD}}$ is the time-varying channel matrix. From Equation (4.3), the received signal matrix can be derived as

$$
\vec{\mathbf{y}} = \mathbf{H}_{\mathrm{TD}} \cdot \vec{\mathbf{x}} + \vec{\nu}
$$

$$
= \mathbf{H}_{\mathrm{TD}} \cdot \left(\mathbf{F}^H \cdot \vec{\mathbf{X}} \right) + \vec{\nu}. \tag{4.4}
$$

In the above equation, $\mathbf{F}$ is the N-dimensional DFT matrix, and it can be written as

$$
\mathbf{F}(n,k) = \frac{1}{\sqrt{N}} e^{-j\frac{2\pi}{N}nk}, \ 0 \le n \le N-1, \ 0 \le k \le N-1 \tag{4.5}
$$

Here, the frequency domain channel matrix, $\mathbf{H}_{\mathrm{FD}}$, is defined as

$$
\mathbf{H}_{\mathrm{FD}} = \mathbf{F} \cdot \mathbf{H}_{\mathrm{TD}} \cdot \mathbf{F}^H, \tag{4.6}
$$

For the ISI free case, the delay spread of the channel is shorter than the length of CP. After removing the ISI corrupted guard interval, the received sequence computes an N-point DFT operation to obtain the frequency domain signal. Therefore, Equation (4.4) can be rewritten as

$$\vec{\mathbf{Y}} = \mathbf{F} \cdot \vec{\mathbf{y}} = \mathbf{F} \cdot \left(\mathbf{H}_{\text{TD}} \cdot \vec{\mathbf{x}} + \vec{\nu} \right)$$

$$= \left(\mathbf{F} \cdot \mathbf{H}_{\text{TD}} \cdot \mathbf{F}^H \right) \cdot \vec{\mathbf{X}} + \mathbf{F} \cdot \vec{\nu}$$

$$\triangleq \mathbf{H}_{\text{FD}} \cdot \vec{\mathbf{X}} + \vec{\mathbf{V}}, \tag{4.7}$$

where $\mathbf{H}_{\text{FD}}$ has the form

$$\mathbf{H}_{\text{FD}} = \begin{bmatrix} H_{\text{FD}}(0,0) & \cdots & H_{\text{FD}}(0,N-1) \\ \vdots & \ddots & \vdots \\ H_{\text{FD}}(N-1,0) & \cdots & H_{\text{FD}}(N-1,N-1) \end{bmatrix}. \tag{4.8}$$

Denote $\mathbf{H}_{\text{FD}}$ as an "equivalent frequency domain channel matrix." In time-varying environments, non-diagonal elements of $\mathbf{H}_{\text{FD}}$ are not zero, and these elements induce the ICI. Let $H_{\text{FD}}(d,k)$ is the d-th row, k-th column of $\mathbf{H}_{\text{FD}}$. Defined $H_{\text{FD}}(d,k) = h_{\text{FD}}(d-k,k)$, where

$$h_{\text{FD}}(d,k) \equiv \frac{1}{N} \sum_{n=0}^{N-1} \sum_{l=0}^{N-1} h_{n,l} e^{-j\frac{2\pi}{N}(lk+dn)}. \tag{4.9}$$

4.1.2 Analysis of ICI Power

In time-invariant channels, the matrix of $\mathbf{H}_{\text{FD}}$ in Equation (4.8) is a diagonal matrix, thus the received signals can be compensated with a simple one-tap equalizer per subcarrier. But in time-varying channels, the matrix of $\mathbf{H}_{\text{FD}}$ is no longer a diagonal matrix, and if one-tap equalizers are still used, the signals will be probably detected

into wrong decisions. Therefore, the non-diagonal terms in the matrix $\mathbf{H}_{\text{FD}}$ (ICI terms) should be mitigated to obtain a set of more reliable decisions.

The ICI power based on the theorem in [5], [20], [25] will be analyzed here. Assuming a typical WSSUS channel model as below

$$E\left\{h_{n,l} \cdot h^{*}_{(n-q),(l-m)}\right\} = \phi_{hh}\left(q \cdot T_s\right)\sigma_l^2 \delta\left(m\right), \tag{4.10}$$

where $\phi_{hh}\left(q \cdot T_s\right) = J_0\left(2\pi f_d \cdot q \cdot T_s\right)$ denotes the normalized tap autocorrelation, T_s is sampling time, and σ_l^2 denotes the variance of the l-th tap. Since the non-diagonal terms of $\mathbf{H}_{\text{FD}}$ are the ICI terms, we will compute the power of these ICI terms. Denote $u(n)$ an N-point rectangular window

$$u(n) = \begin{cases} 1, & 0 \leq n \leq N, \\ 0, & \text{else.} \end{cases} \tag{4.11}$$

Use Equation (4.9), Equation (4.10), and $u(n)$, the ACF of $h_{\text{FD}}\left(d,k\right)$ can be expressed as

$$E\left\{\left|h_{\text{FD}}\left(d,k\right)\right|^2\right\} = \frac{1}{N^2}\sum_{n,l,m,p} u(n)\,u(m)\,E\left\{h_{n,l}h^{*}_{m,p}\right\}e^{j\frac{2\pi}{N}(pk-lk+md-nd)}$$

$$= \frac{1}{N^2}\sum_{l}\sigma_l^2\sum_{n,m} u(n)\,u(m)\,\phi_{hh}\left((n-m)\cdot T_s\right)e^{j\frac{2\pi}{N}(md-nd)}$$

$$= \frac{1}{N^2}\sum_{l}\sigma_l^2\sum_{q}\sum_{n} u(n)\,u(n-q)\,\phi_{hh}\left(q \cdot T_s\right)e^{-j\frac{2\pi}{N}qd} \tag{4.12}$$

Further define the (2N-1)-point triangular window

$$r(q) \equiv \begin{cases} N - |q|, & -N < n < N, \\ 0, & \text{else.} \end{cases} \tag{4.13}$$

Equation (4.12) can be rewritten as

$$E\left\{\left|h_{\text{FD}}(d,\cdot)\right|^2\right\} = \frac{1}{N^2}\sum_l\sigma_l^2\sum_q r(q)\phi_{hh}(q\cdot T_s)e^{-j\frac{2\pi}{N}qd}$$

$$= \left\{S(f)*\left(\frac{1}{N^2}\sum_q\phi_{hh}(q\cdot T_s)e^{-jf\cdot q}\right)\right\}_{f=\frac{2\pi}{N}d}\cdot\sum_l\sigma_l^2, \tag{4.14}$$

where $S(f)$ is shown in Equation (3.14).

From Equation (4.14), the ICI variance $E\{|h_{\text{FD}}(d,\cdot)|^2\}$ versus d is simulated. Figure 4.1 shows the computer simulations according to Equation (3.14) and Equation (4.14). From Figure 4.1, we can find the coefficients of the frequency domain channel matrix have the most power on the central band and the edges of the channel matrix. When the maximum Doppler shift increases, more signal power leaks out to the neighboring subcarriers. Therefore, by the relations between the ICI power and the maximum Doppler shift, we can know how many neighboring subcarriers should be taken account to the ICI eliminating procedure.
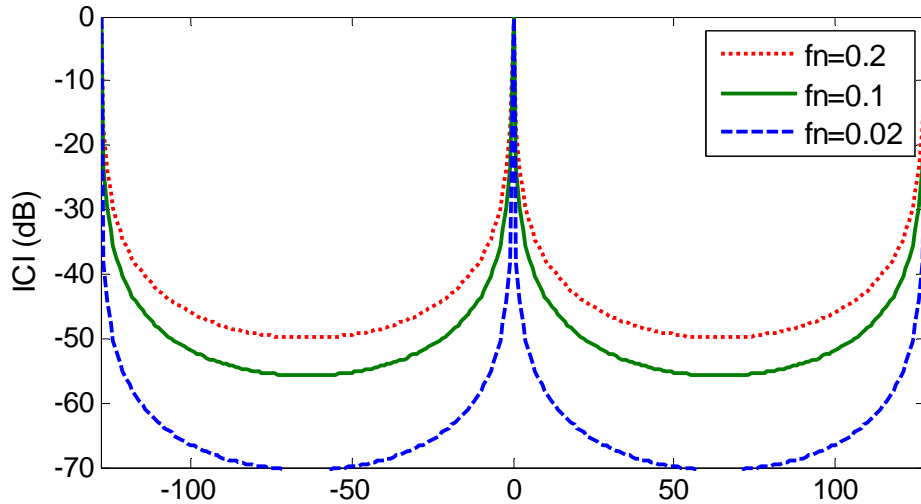

Figure 4.1 (a): ICI variance versus d (d is the index of super- or sub- diagonal)
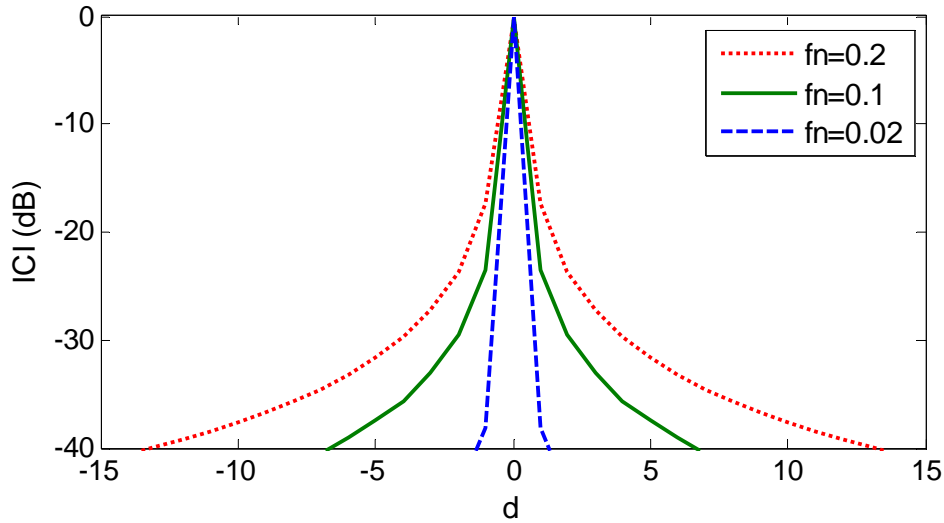
Figure 4.1 (b): Zoomed view of Figure 4.1 (a)

4.2 Adaptive ICI Cancellation Scheme

In this session, we will introduce an adaptive ICI cancellation scheme based on [5], which provides a low-complexity linear minimum mean square error (LMMSE) estimator. According to the analysis in Section 4.1, we can know that the main ICI comes form the several neighboring subcarriers. In order to reduce the computational complexity and memory size requirement, we can only use some elements of matrix $\mathbf{H}_{FD}$. Therefore, to squeezes the significant coefficient of $\mathbf{H}_{FD}$ (Equation 4.7) into the $2D+1$ central diagonals, a $D \times D$ lower triangular matrix in the bottom-left corner, and a $D \times D$ upper triangular matrix in the top-right corner, illustrated in Figure 4.2. It shows that the desired structure of $\mathbf{H}_{FD}$ which passes the shaded region and zeros the non-shaded region. When the maximum Doppler shift is given, the value of D can be determined. The parameter D can be chosen to tradeoff between the performance and the complexity. The choice of parameter D will be described later in Section 4.3.
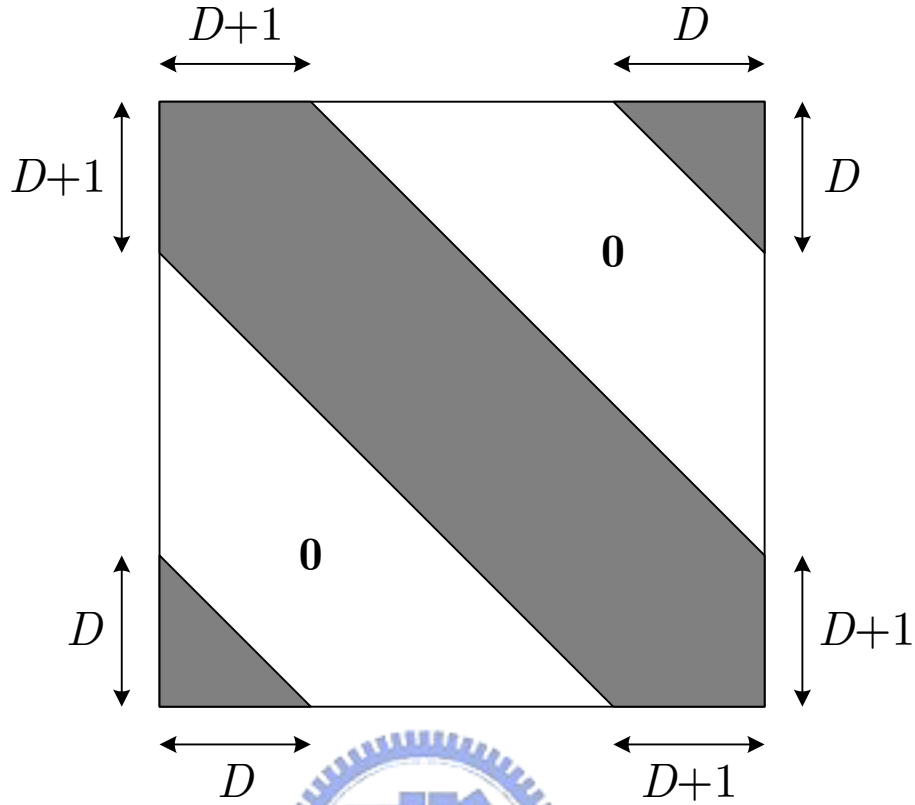
Figure 4.2: Desired structure of frequency domain channel matrix

4.2.1 Low-Complexity MMSE ICI Cancellation

With linear time-invariant channels, $\mathbf{H}_{\mathrm{FD}}$ is diagonal, and the LMMSE equalization scheme can be implemented in $O(N)$ operations. This simple frequency domain equalization is the conventional motivation for the use of OFDM. However, with time-invariant channels, $\mathbf{H}_{\mathrm{FD}}$ is not diagonal any more, the LMMSE estimator requires matrix inversion. In classical method, the LMMSE estimator [11], [12] is given by

$$\vec{\mathbf{X}} = \left(\mathbf{H}_{\mathrm{FD}}^{H} \cdot \mathbf{H}_{\mathrm{FD}} + N_0 \mathbf{I} \right)^{-1} \mathbf{H}_{\mathrm{FD}}^{H} \cdot \vec{\mathbf{Y}} \qquad (4.15)$$

The implementation of the MMSE estimator requires $O\left(N^3\right)$ operations, resulting in impractical implementation for large N. The major computation in Equation (4.15) is in calculation the inverse. In order to reduce the computational complexity, a low-complexity MMSE equalizer [5] is used here.

The low-complexity LMMSE estimator is applied to reduce the ICI and noise. Using parameter D to determine the desired structure of frequency domain channel matrix, we can obtain

$$\widehat{\mathbf{H}}_{\text{FD}} = \mathbf{C}_{\text{M}} \cdot \mathbf{H}_{\text{FD}} \tag{4.16}$$

where $\mathbf{C}_{\text{M}}$ denotes a mask matrix that pass the shaded region and zeros the non-shaded region in Figure 4.2. Let $U = 2 \cdot D + 1$, and a $U \times 1$ vector with i-th entry is defined $[\vec{\mathbf{r}}_u]_i \triangleq [(u - D - 1 + i) \mod N] + 1, \; i = 1, \cdots, U$. From Equation (4.7), we have

$$\vec{\mathbf{Y}}_u = \widehat{\mathbf{H}}_{\text{FD},u} \cdot \vec{\mathbf{X}} + \vec{\mathbf{V}}_u, \tag{4.17}$$

where $\vec{\mathbf{Y}}_u = \vec{\mathbf{Y}}(\vec{\mathbf{r}}_u)$, $\widehat{\mathbf{H}}_{\text{FD},u} = \widehat{\mathbf{H}}_{\text{FD}}(\vec{\mathbf{r}}_u,:)$, and $\vec{\mathbf{V}}_u = \vec{\mathbf{V}}(\vec{\mathbf{r}}_u)$. The MMSE estimator for detecting based on Equation (4.17) is $\mathbf{b}_u = \mathbf{R}_u^{-1}\mathbf{p}_u$, where $\mathbf{R}_u = E\{\vec{\mathbf{Y}}_u \cdot \vec{\mathbf{Y}}_u^H\} = \widehat{\mathbf{H}}_{\text{FD},u} \cdot \widehat{\mathbf{H}}_{\text{FD},u}^H + N_0 \mathbf{I}_u$, and $\mathbf{p}_u = \widehat{\mathbf{H}}_{\text{FD}}(:,u)$. Since the first $U - 1$ rows of $\mathbf{R}_{u+1}$ and the last $U - 1$ rows of $\mathbf{R}_u$ are the same, the inverse of $\mathbf{R}_u$ can be recursively calculated, and the computational complexity can be greatly reduced. The total computational complexity of this low-complexity method is only $O\left(N^2 U\right)$ operations [5]. On the other hand, using an MMSE receiver based on the whole frequency domain channel matrix, as suggested in [24], requires $O\left(N^3\right)$ operations. Since $U \ll N$, the computational complexity decreases greatly.

4.3 Computer Simulations

In this section, the simulation results of the adaptive ICI cancellation scheme will be presented. The simulation parameters are listed in Table 4.1. The channel model is the Jakes model. The normalized maximum Doppler shift f_n is changed between 0 and 0.15. The configuration we consider here is an OFDM system with a bandwidth of 6 MHz and 2K mode of DVB-T systems. The QPSK modulation scheme is adopted in the below simulations. Through out simulations, the timing synchronization and channel state information (CSI) are assumed to be known. Here, we still used the proposed maximum Doppler shift estimation method to estimated Doppler shift. Moreover, The CTA method is used and the observation interval K is 128 symbols with $Q = 5$. The maximum frequency difference Δf_{max} is 50 Hz.

Table 4.1: Parameters of computer simulations

System	DVB-T
Transmission mode	2K
Channel bandwidth	6 MHz
CP length	1/4 OFDM symbol
Modulation	QPSK
Carrier frequency	710 MHz
Normalized maximum Doppler shift	0 ~ 0.15
Channel model	Jakes model

Figure 4.3 to Figure 4.7 compare the BER performance of the low-complexity MMSE and the conventional one-tap equalizer for different normalized Doppler shift. The performance of the known CSI is also shown in these figures. If the parameter D of the low-complexity MMSE increases, the BER performance improves correspondingly. In Figure 4.3, when the normalized maximum Doppler shift is smaller than 0.01, the MMSE and the one-tap equalizer both have the similar BER performance. When the Doppler shift increased, more signal power leaks out to the neighboring subcarriers. Therefore, the parameter D must be appropriately chosen to maintain the BER performance under a desired level.

Figure 4.3: BER performance versus SNR. The normalized maximum Doppler shift is 0.01.

Figure 4.4: BER performance versus SNR. The normalized maximum Doppler shift is 0.05.
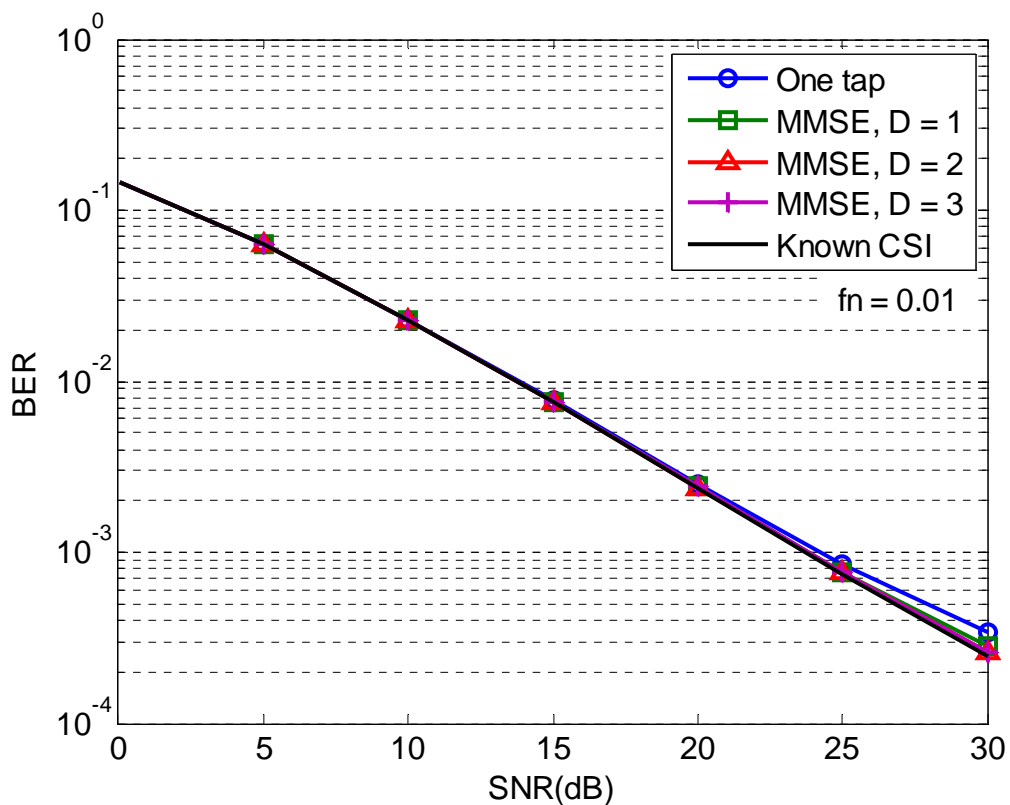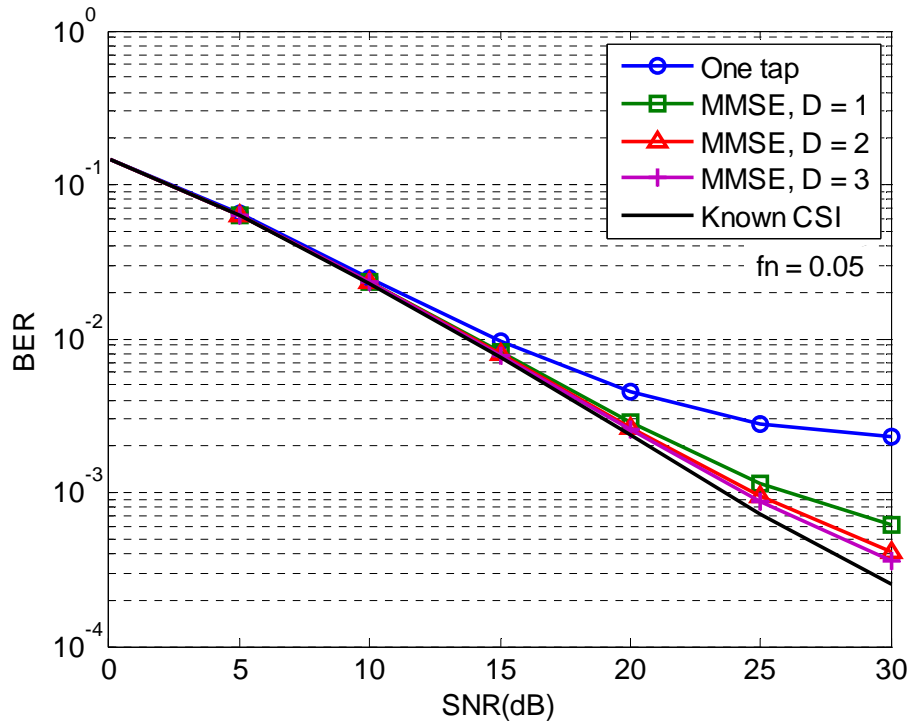

Figure 4.5: BER performance versus SNR. The normalized maximum Doppler shift is 0.1.

Figure 4.6: BER performance versus SNR. The normalized maximum Doppler shift is 0.15.
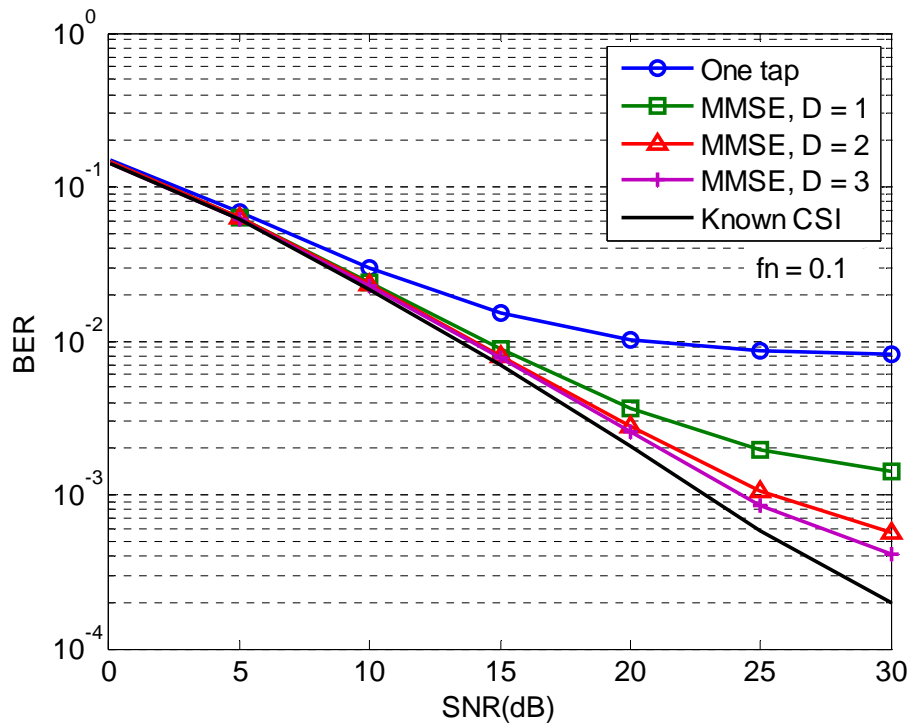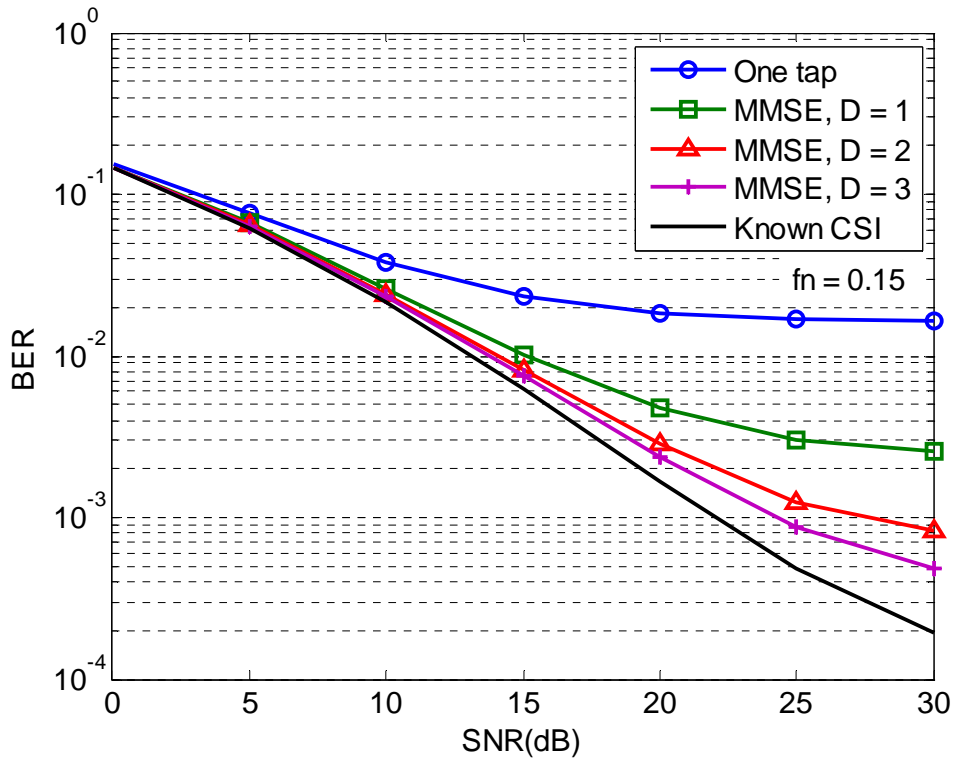
An adaptive ICI cancellation scheme can be achieved, because the information of the maximum Doppler shift is known by the estimation. A threshold scheme is proposed to provide a tradeoff between the performance and the computational complexity. For example, we choose that the BER performance is smaller than 10^{-3} in SNR = 25 dB. Therefore, the threshold of the adaptive ICI cancellation scheme can be determined by using the above simulation results. Table 4.2 lists the thresholds and their corresponding equalization type. When the normalized maximum Doppler shift is equal to or smaller than 0.01, the one-tap equalization can sufficiently satisfy the requirement. But, if the normalized maximum Doppler shift is larger than 0.01, the MMSE equalization with appropriate parameter D is needed such that the BER performance can be hold.

Table 4.2: Adaptive ICI cancellation scheme

Normalized max. Doppler shift	Equalizer
$f_n \leq 0.01$	One-tap equalizer
$0.01 < f_n \leq 0.05$	MMSE with $D = 1$
$0.05 < f_n \leq 0.1$	MMSE with $D = 2$
$0.1 < f_n$	MMSE with $D = 3$

Figure 4.7 shows the BER performance of different equalization type with variation of normalized maximum Doppler shift, which shows in Figure 4.8. As the result in Figure 4.7, the BER performance of the adaptive ICI cancellation scheme is better than the BER performance of the MMSE with $D = 2$. Although the BER performance of the MMSE with $D = 3$ is better than other equalization types, the computational complexity of the MMSE with $D = 3$ is larger than others. The maximum average computational complexity per OFDM symbol of the MMSE with $D = 3$ and the MMSE with $D = 2$ is respectively $O\left(7N^2\right)$ and $O\left(5N^2\right)$ operations; the maximum average computational complexity per OFDM symbol of the adaptive method is about $O\left(4.71 \cdot N^2\right)$ operations, as shown in Figure 4.9. As can be seen, the MMSE with $D = 3$ and the MMSE with $D = 2$ waste the computational complexity and processing time in low Doppler shift ($f_n < 0.05$), rather than improve the BER performance appreciably. The adaptive ICI cancellation scheme can use the appropriate computational complexity, and satisfies the performance requirement.
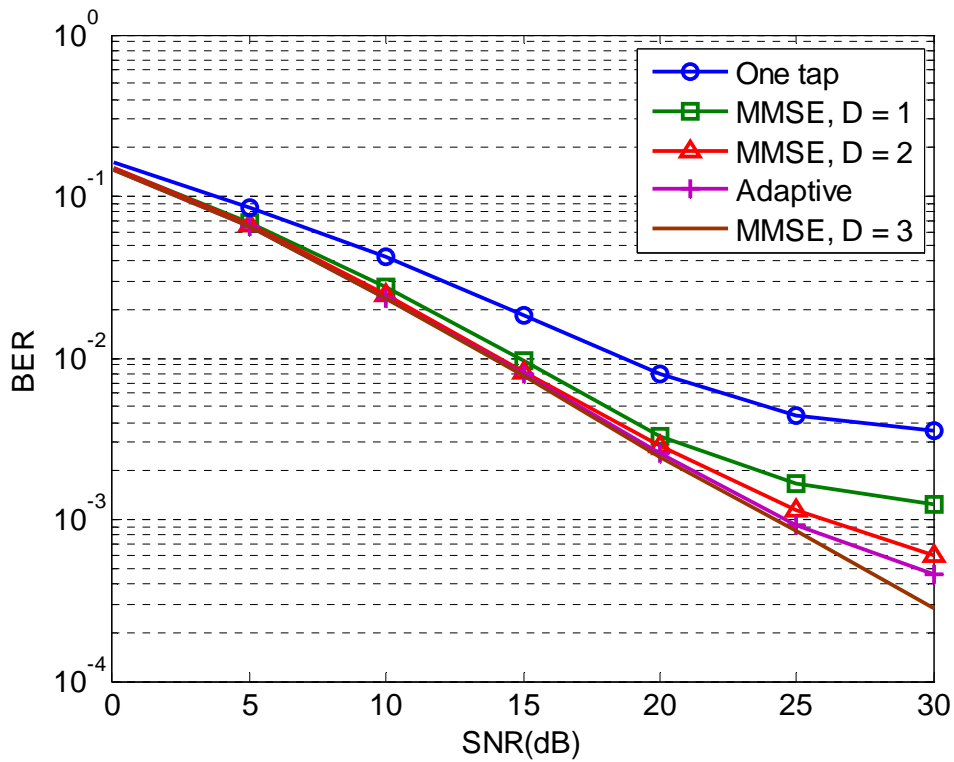
Figure 4.7: BER performance of different equalization type with variation of normalized maximum Doppler shift.
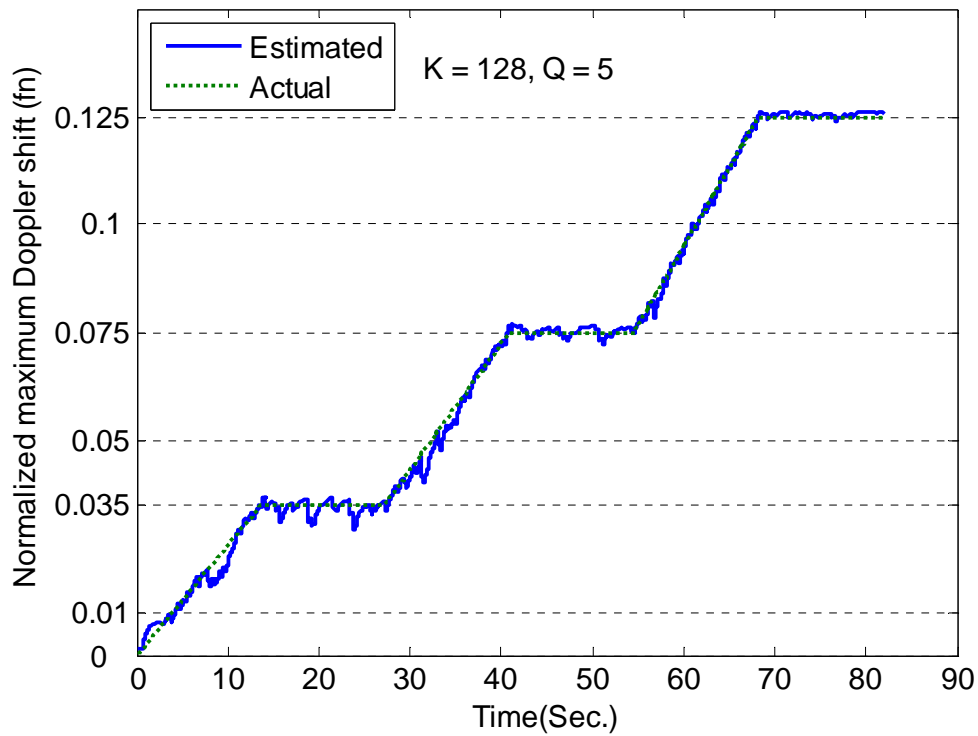

Figure 4.8: Variation of normalized maximum Doppler shift for Figure 4.7.
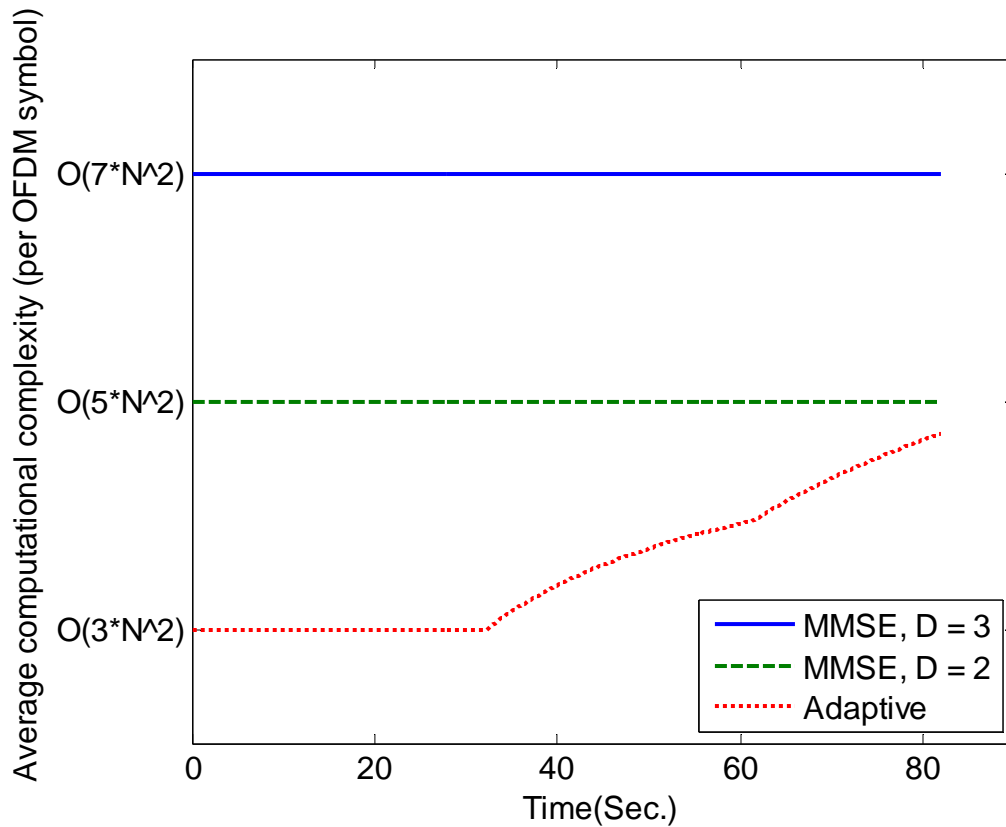
Figure 4.9: Average computational complexity of MMSE with $D = 3$, MMSE with $D = 2$, and the adaptive ICI cancellation scheme

4.4 Summary

In this chapter, the ICI analysis is introduced and shows the relation between ICI and the maximum Doppler shift. By this relation and simulation results, we can know that how many neighboring subcarriers should be taken account to the ICI eliminating procedure. Therefore, an adaptive ICI cancellation scheme be proposed, and this method can use the appropriate computational complexity to mitigate the ICI effects.

Chapter 5

Conclusion

In this thesis, we proposed a maximum Doppler shift estimation method for mobile OFDM systems. This proposed method can work well over a wide Doppler shift range at low SNR. Moreover, it can provide more flexibility between the estimation accuracy and computational complexity by changing the observation interval and accumulation size. In Chapter 2, the technique of OFDM systems and DVB systems were introduced. In Chapter 3, the proposed maximum Doppler shift estimation method was presented. This method employs the characteristics of Doppler power spectrum, which is the frequency domain of the ACF of the estimated CIRs. Moreover, the FFT scheme and the CTA scheme were proposed, and these two schemes provide a tradeoff between the computational complexity and the memory size requirement. Then, the complexity of these schemes is analyzed; the FFT scheme has lower computational complexity than the CTA scheme, but it needs a larger memory size than the CTA scheme. To reduce the variation of noise and interference power spectrum, the estimated Doppler power spectrum is accumulated. When the proposed method utilizes a larger observation interval and accumulation size, the estimation results achieve a better accuracy and work well at low SNR. In Chapter 4, ICI analysis and an adaptive ICI cancellation scheme were presented. When the maximum Doppler shift increases,

more signal power leaks out to the neighboring subcarriers. By the relations between the ICI power and the maximum Doppler shift, we can know how many neighboring subcarriers should be taken account to the ICI eliminating procedure. Therefore, the adaptive method can utilize the appropriate equalizer to mitigate ICI as the maximum Doppler shift is given. Then, we analyze the complexity of the adaptive ICI cancellation scheme and compare this scheme with other schemes.

In new generation wireless communication systems, OFDM systems are considered for both fixed and mobile environment. Those new generation systems should be capable of working efficiently in a wide operating range, such as different carrier frequencies in licensed and licensed-exempt bands, large speeds rang of subscribers. The above reasons motivated the use of adaptive techniques, and one key parameter in adaptive mobile communication systems is the maximum Doppler shift. Knowing Doppler shift also can aid handoffs and power control. Therefore, our goal is to combine the proposed maximum Doppler shift estimation method with these applications in the future work.

Bibliography

[1] ETSI, "Digital video broadcasting (DVB); framing structure, channel coding and modulation for digital terrestrial television," ETSI EN 300 744, Nov. 2004.

[2] M. Speth, S. A. Fechtel, G. Fock, and H. Meyr, "Optimum receiver design for wireless broad-band systems OFDM－part I," *IEEE Trans. Commum.*, vol. 47, no. 11, pp. 1668-1677, Nov. 1999.

[3] M. Speth, S. A. Fechtel, G. Fock, and H. Meyr, "Optimum receiver design for wireless broad-band systems OFDM － part II: a case study," *IEEE Trans. Commum.*, vol. 49, no. 4, pp. 571-578, Apr. 2001.

[4] ETSI, "Digital video broadcasting (DVB); transmission system for handheld terminals (DVB-H)," ETSI EN 302 304, Nov. 2004.

[5] X. Cai, and G. B. Giannakis, "Bounding performance and suppressing intercarrier interference in wireless mobile OFDM," *IEEE Trans. on Commum.*, vol. 51, no. 12, pp. 2047-2056, Dec. 2003.

[6] A. Sampath and J. M. Holtzman, "Estimation of maximum Doppler frequency for handoff decisions," in *Proc. IEEE Veh. Tech. Conf.*, pp. 859-862, 1993.

[7] L. Krasny, H. Arslan, D. Koilpillai, and S. Chennakeshu, "Doppler spread estimation in mobile radio systems," *IEEE Commun. Lett.*, vol. 5, no. 5, pp. 197-199, May. 2001.

[8] H. Arslan, L. Krasny, D. Koilpillai, and S. Chennakeshu, "Doppler spread estimation for wireless mobile radio systems," in *Proc. IEEE Wireless Communications and Networking Conf.*, vol. 3, pp. 1075-1079, 2000.

[9] J. Cai, W. Song, and Z. Li, "Doppler spread estimation for mobile OFDM systems in Rayleigh fading channels," *IEEE Trans. Consumer Electron.*, vol. 49, pp. 973-977, Nov. 2003.

[10] G. Park, D. Heo, D. Hong, and C. Kang, "A new maximum Doppler frequency estimation algorithm in frequency domain," in *Proc. IEEE Communication Systems, ICCS 2002. The 8th International Conf.*, vol. 1, pp. 548-552, Nov. 2002.

[11] A.A. Hutter, R. Hasholzner, and J.S. Hammerschmidt, "Channel estimation for mobile OFDM systems," in *Proc. IEEE Veh. Tech. Conf.*, vol. 1, pp. 305-309, Sep. 1999.

[12] K. Chang, K. Kim, and D. Kim, "Reduction of Doppler effects in OFDM systems," *IEEE Trans. Consumer Electron.*, vol. 52, no. 4, pp. 1159-1166, Nov. 2006.

[13] R. van Nee and R. Prasad, *OFDM for Wireless Multimedia Communication*, Artrch House, 2000.

[14] H. Benoit, *Digital television: MPEG-1, MPEG-2 and principles of the DVB system*, *2nd ed*., Focal Press, 2002.

[15] M. Massel, *Digital television :DVB-T COFDM and ATSC 8-VSB*, Digitaltvbooks.Com, 2000.

[16] Y. Zhao, A. Huang, "A novel channel estimation method for OFDM mobile communication systems based on pilot signals and transform-domain processing." in *Proc. IEEE Veh. Tech. Conf.*, pp. 2089-2093, 1997.

[17] W. C. Jakes, *Microwave Mobile Communications*. Piscataway, NJ: IEEE Press, 1993.

[18] G. L. Stbüer, *Principles of Mobile Communication, 2nd ed.*, Norwell, MA: Kluwer Academic Publishers, 2001.

[19] T. Yücek, R. M. A. Tannious and H. Arslan, "Doppler spread estimation for wireless OFDM systems," in *Proc. IEEE Sarnoff Symp. Wired and Wireless Communication,* pp. 233-236, Apr. 2005.

[20] P. Schniter, "Low-complexity equalization of OFDM in doubly selective channels," *IEEE Trans. Signal Processing*, vol. 52, pp. 1002-1011, Apr. 2004.

[21] R. Negi and Cioffi, "Pilot tone selection for channel estimation in a mobile OFDM system," *IEEE Trans. Consumer Electron.*, vol. 44, pp. 1122-1128, Aug. 1998.

[22] Y. Mostofi, and D. C. Cox, "ICI mitigation for pilot-aided OFDM mobile systems," *IEEE Trans. Wireless Commum.*, vol. 4, no. 2, pp. 765-774, Mar. 2005.

[23] A. V. Oppenheim, and R. W. Schafer, *Discrete-Time Signal Processing, 2nd ed.*, Upper Saddle River, NJ: Prentice-Hall, 1999.

[24] Y. S. CHoi, P. J. Voltz, and A. C. Cassara, "On channel estimation and detection for multicarrier signals in fast and selective Rayleigh fading channels," *IEEE Trans. Commum.*, vol. 49, no. 8, pp. 1375-1387, Aug. 2001.

[25] W. G. Jeon, K. H. Chang, Y. S. Cho, "A equalization technique for orthogonal frequency-division multiplexing systems in time-variant multipath channels," *IEEE Trans. on Commum.*, vol. 47, pp. 27-32, Jan. 1999.